RESEARCH | Article in Press

Inflammatory macrophages promote metastatic potential in triple-negative breast cancer through integrated stress response signaling

Martina Crippa · Vincenzo Salemme · Jagat Chauhan · Emanuele Colombo · Alessia Loffreda · Alessia Lamolinara · Clara Cardella · Martina Leone · Eugenia Licari · Marco Gaviraghi · Francesca Genova · Achille Anselmo · Davide Mazza · Manuela Iezzi · Colin Goding · Paola Defilippi · Carlo Tacchetti · Paola Falletta

Received: 6 May 2026 / Accepted: 28 August 2026

Abstract

Triple-negative Breast Cancer (TNBC) is characterized by inflammatory myeloid infiltration and a high metastatic potential, however, the mechanisms by which macrophage-derived signals govern tumor cell plasticity remain poorly understood. Here, through patient transcriptomic analyses, in vitro functional studies, and in vivo metastasis models, we identify the Integrated Stress Response (ISR) as a critical tumor cell-intrinsic pathway that translates inflammatory macrophage-derived cues into metastatic competence. In breast cancer clinical cohorts, ISR programs are enriched in TNBC and associate with poor outcome and inflammatory macrophage infiltration. Functionally, we show that the inflammatory macrophage secretome triggers ISR-dependent invasion in TNBC cells. Mechanistically, we identify CXCL10 as a macrophage-derived mediator necessary and sufficient to induce ISR activation and invasion through CXCR3 receptor. Finally, we demonstrate that tumor-intrinsic ISR signaling promotes TNBC metastatic dissemination in vivo. Together, our findings establish a macrophage-CXCL10-CXCR3-ISR signaling axis that fuels metastatic behavior in TNBC and identify this pathway as a potential node for therapeutic intervention.

Statement of significance Inflammatory macrophages promote TNBC metastasis by activating the Integrated Stress Response via a CXCL10-CXCR3 paracrine loop. These results bridge the gap between inflammation and tumor-intrinsic stress signaling, uncovering a novel mechanistic axis for therapeutic intervention.

Keywords Triple-negative breast cancer (TNBC) · Tumor-associated macrophages (TAMs) · Integrated stress response (ISR) · CXCL10-CXCR3 axis · Macrophage secretome · 3D microfluidic invasion assay · Invasion and metastasis

Carlo Tacchetti and Paola Falletta are co-last authors.

Introduction

Metastasis is the leading cause of cancer-related death [1] and the major determinant of poor outcome across solid tumors [2]. Successful dissemination requires cancer cells to survive hostile conditions and engage the molecular programs required for distant organs colonization [3–5]. These traits are shaped both by intrinsic genetic alterations and by sustained crosstalk with the tumor microenvironment (TME) which provides metabolic, inflammatory, and mechanical stimuli that can either constrain or promote malignant progression [6–8]. Accordingly, signaling pathways that integrate these extrinsic inputs into tumor cell programs of stress adaptation, plasticity and invasion are particularly attractive both mechanistically and therapeutically, as they represent the molecular bridge between microenvironmental dependencies and metastatic fitness. Among them, the Integrated Stress Response (ISR) has emerged as a compelling regulator of plasticity and invasion [9–11].

The ISR is an evolutionarily conserved signaling network that enables cells to respond to diverse intrinsic and extrinsic stresses by regulating protein synthesis through phosphorylation of eukaryotic translation initiation factor 2 subunit 1 (eIF2α) [12]. This translation reprogramming attenuates global cap-dependent protein synthesis while selectively enhancing translation of a subset of stress-responsive mRNAs, including the key effector of the ISR, Activating transcription factor 4 (ATF4) [13, 14]. In physiology, the ISR functions as a guardian of cellular homeostasis, coordinating decision between adaptation and cell death depending on the nature, intensity and duration of stress, as well as the capacity of a specific cell to endure it [15, 16]. In cancer, however, the adaptive counterpart of this program can be hijacked to promote tumor progression.

We and others have highlighted a pivotal role for the ISR in metastasis, particularly in the acquisition of invasive traits in tumor cells [9, 17, 18]. ISR activation can rewire cancer cell behavior, inducing a phenotype switch to favor dissemination [19]. Collectively, this body of evidence suggests the ISR as a candidate regulator of tumor-TME crosstalk during metastatic progression. However, the tumor contexts in which ISR programs are most relevant, and the microenvironmental cues that drive them during dissemination, are not yet fully determined.

Triple-negative Breast Cancer (TNBC) provides a clinically relevant context in which to investigate stress-adaptive programs linked to metastasis. Defined by the absence of estrogen receptor (ER) and progesterone receptor (PR) expression and lack of HER2 amplification, TNBC accounts for 15–20% of breast cancers yet contributes disproportionately to mortality because of its high metastatic propensity and the limited availability of targeted treatment options [20]. Beyond its clinical relevance, TNBC is characterized by a marked cellular plasticity and a tumor microenvironment enriched in inflammatory and immune-derived signals [21]. Yet the determinants and consequences of ISR activation in this context remain poorly defined.

Within the TNBC microenvironment, tumor-associated macrophages (TAMs) represent one of the most abundant, plastic and functionally influential immune cell populations [22]. TAMs shape tumor evolution and therapeutic response through context-dependent effects on cancer cells and the stromal environment [23, 24]. In TNBC, macrophage-rich inflammatory states have been associated with aggressive disease, raising the possibility that macrophage-derived signals may directly contribute to the metastatic phenotype [25, 26]. TAMs can be conceptualized along a functional continuum from pro-inflammatory, cytotoxic “M1-like” to immunosuppressive, pro-metastatic “M2-like” states, yet their plasticity in vivo enables a nuanced and context-dependent reprogramming [27, 28]. Although this binary framework only partially captures the diversity and plasticity of macrophage states in vivo, it nonetheless underscores the capacity of local cytokine milieus to dynamically reprogram macrophage functions, which in turn acquire the capability to drive disease trajectories. In particular, inflammatory cytokines (e.g., IFNγ, TNFα) as well as wound-healing cytokines (IL-4/IL-13) are established drivers of distinct macrophage activation states and, within tumors, the local balance between these cues contributes to the dynamic tuning of TAM function [29–31].

The inflammatory microenvironment represents a plausible source of the extrinsic signals capable of engaging adaptive tumor cell programs. However, whether inflammatory macrophages directly activate the ISR in TNBC,

through which molecular mediators, and with what functional consequences for metastatic progression, has not been established.

Here, we combine transcriptomic, mechanistic and in vivo approaches to define an inflammatory macrophage-to-tumor signaling axis that activates the ISR in breast cancer cells. We identify a pro-inflammatory macrophage secretory program that engages the ISR in tumor cells and promotes invasive behavior, and we delineate the CXCL10-CXCR3 axis as a critical mediator of this response. Finally, we show that tumor cell-intrinsic ISR signaling contributes to metastatic competence in vivo.

Results

ISR programs identify TNBC as a distinct inflammatory breast cancer subtype

BC cell adaptation to microenvironmental pressures is a key determinant of tumor progression and metastasis. By integrating diverse stress signals into a translational and transcriptional program that enhances tumor cell plasticity, the ISR acts as a central hub that shapes the aggressive BC phenotype.

To define the clinical and biological context of ISR activation in BC, we examined two independent transcriptional signatures that capture activation across distinct stress cues and cancer models: a canonical "Metabolic Stress" signature derived from melanoma cells under glutamine starvation [9], and a newly derived "Chemical Stress" signature generated in biological triplicate from MDA-MB-231 cells following pharmacological ISR induction with the eIF2α phosphatase Sephin1 [32] (Supplementary Table 1). Notably, although the two ISR signatures do not share genes, their scores were positively correlated across the TCGA-BRCA primary breast tumors cohort (Fig. S1A), indicating convergence on a common stress-associated state. In METABRIC, a large and clinically annotated breast cancer cohort comprising approximately 2000 primary tumors with genomic, transcriptomic and long-term outcome data [33], high Metabolic Stress scores were associated with poorer overall survival (OS), diseases-specific survival (DSS) and relapse-free survival (RFS) (Fig. 1A-C), while in TCGA-BRCA OS analysis independently identified the adverse prognostic association (Fig. S1B), supporting the clinical relevance of ISR-linked transcriptional states in BC.

Because ISR programs, together with established ISR-related genes such as ATF4 and its canonical transcriptional target asparagine synthetase ASNS [34], were preferentially enriched in TNBC compared to other breast cancer subtypes (Fig. 1D; Fig S1C-D), we prioritized TNBC for downstream mechanistic investigation.

Consistent with our previous observation that ISR activation promotes metastatic potential [9], pre-ranked GSEA of both ISR programs identified epithelial-to-mesenchymal transition (EMT) among the highest positively enriched Hallmark pathways in TCGA-BRCA (Fig. 1E; Fig S1E), providing independent clinical transcriptomic support for ISR-associated invasiveness. Both signatures were also strongly associated with inflammatory pathways, including TNFα signaling via NFκB, inflammatory response, IL6-JAK-STAT3 signaling and interferon response (Fig. 1E; Fig S1E), suggesting that ISR-high tumors are embedded in a pro-inflammatory microenvironment.

To assess whether the relationship between ISR-related programs and microenvironmental cues extended beyond glutamine deprivation, we examined additional MSigDB-derived signatures representing glucose deprivation, hypoxia, response to acidic pH, glycolysis, oxidative stress, heat stress and osmotic stress (Supplementary Table 1). The Metabolic and Chemical Stress programs correlated positively with most of the signatures, with hypoxia showing the strongest association (Fig. S1F). These microenvironmental stress programs were also enriched in TNBC relative to the other BC subtypes (Fig. S1G). Response to acidic pH was a notable exception: it neither correlated with the ISR-related reference signatures nor showed TNBC enrichment. Because the signature is dominated by proton sensing receptors and ion channels, it may capture pH detection and adaptation, and since response to acidic pH has been associated with reduced

https://doi.org/10.1186/s13046-026-03821-4

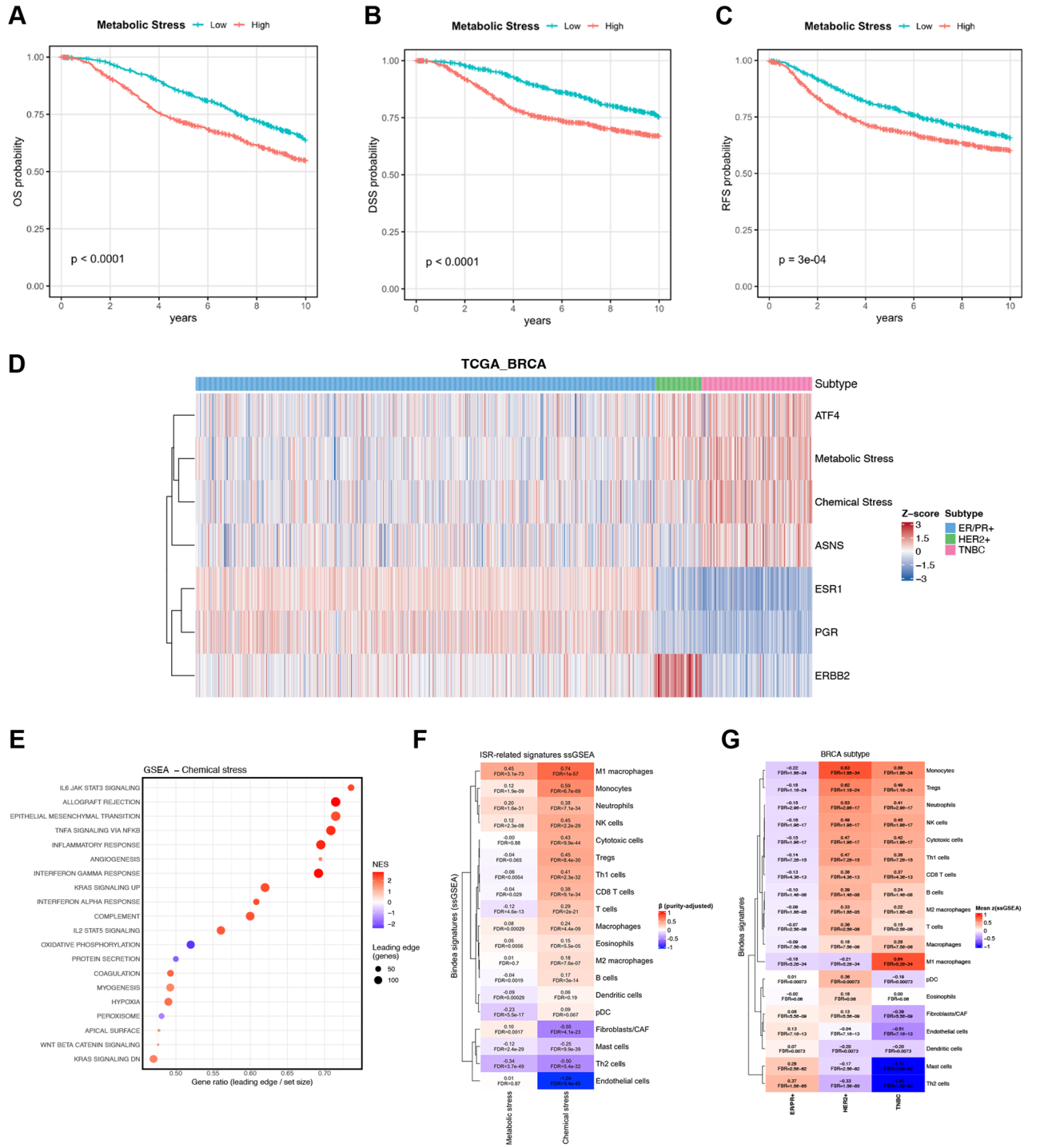

Fig. 1 ISR-associated transcriptional programs identify TNBC as an inflammatory, macrophage-enriched breast cancer subtype. **A-C** Kaplan-Meier analyses in METABRIC comparing tumors with high and low Metabolic Stress signature scores for (**A**) overall survival, (**B**) disease-specific survival, and (**C**) relapse-free survival. Patients were stratified into a high and low expression groups using an optimal cut-point derived by maximally selected rank statistic. *P* values are calculated with two-sided long-rank tests. **D** Hierarchically clustered heatmap showing the z-scored expression of ISR programs (metabolic and chemical) and representative ISR-associated genes (ATF4 and its canonical transcriptional target ASNS) and BC subtype-associated markers across TCGA-BRCA patient samples. Columns represent individual tumors and are grouped by subtype. Values are displayed as per-row-z-scores. **E** Gene set enrichment analysis of the chemical stress signature using the MSigDB Hallmark collection. The x-axis indicates the gene ratio, bubble size represents the number of leading-edge genes, and colors indicate the normalized enrichment score (NES). **F** Hierarchically clustered heatmap of Bindea immune and stromal signatures and ISR programs (metabolic and chemical) scored by ssGSEA. Heatmap color indicates the regression coefficient for each Bindea term, each tile is annotated with b and Benjamini-Hochberg FDR. **G** Hierarchically clustered heatmap of Bindea ssGSEA landscape across TCGA-BRCA subtypes. ssGSEA scores were z-scored per signature across all tumors and averaged within subtype groups. Heatmap colors represent mean z-scored ssGSEA values. Each tile is annotated with the z-score and Benjamini-Hochberg FDR from a Kruskal-Wallis test across subtype groups

glycolytic activity [35], it may represent a cellular state distinct from the hypoxia-glycolysis-ISR axis that predominates BC.

In line with the pro-inflammatory transcriptional landscape, immune-context analysis using the Bindea immune signatures [36] (Supplementary Table 1) showed that ISR activity was most strongly associated with myeloid and cytotoxic immune programs, particularly an M1 macrophage-associated transcriptional program (Fig. 1F). This program was preferentially enriched in TNBC (Fig. 1G), evidencing that TNBC displays the strongest combined enrichment of metabolic stress, chemical stress and M1 macrophages transcriptional programs (Fig. S1H). Moving-average analyses further showed that increased metabolic or chemical stress was accompanied by a parallel increase in the M1 macrophage program across BCs (Fig. S1I-J). Importantly, orthogonal CIBERSORTx-based deconvolution [37] further identified a higher inferred relative abundance of M1 macrophages in TNBC and confirmed its association with ISR-related signatures (Fig. S1K-L). Thus, these analyses support both enrichment of an M1 macrophage-associated transcriptional state and increased relative abundance of M1-like macrophages.

TNBC as an ISR-enriched BC subtype marked by a relevant inflammatory microenvironment and identify M1 macrophages as the immune context most tightly linked to ISR activation. The aggressive clinical behavior of TNBC, characterized by limited therapeutic options and high metastatic propensity, prompted functional studies to test whether macrophage-derived cues directly activate ISR signaling in TNBC cells.

Pro-inflammatory macrophage secretome activates the ISR across breast cancer models

Building upon the transcriptomic link between ISR activation and M1 macrophages in TNBC patient samples, we next functionally tested whether macrophage-derived cues directly activate ISR in TNBC cells. Monocytes isolated from healthy female donor PBMCs were differentiated with M-CSF for 5 days into unpolarized M0 macrophages, then polarized with IFNγ/TNFα to generate a pro-inflammatory M1-like state and IL-4/IL-13 to generate an anti-inflammatory M2-like state (Fig. 2A), thereby modelling sterile intratumoral inflammatory signaling while avoiding bacterial PAMP-driven stimulation such as LPS [38]. Flow-cytometric profiling of canonical markers confirmed effective macrophage polarization (Fig. S2A) while confocal cytoskeletal imaging and ultrastructural electron microscopy analyses further supported distinct macrophage morphologies across states (Fig. S2B-C).

Conditioned media (CM) from each macrophage state were applied to MDA-MB-231 TNBC cells. CM derived from M1-like macrophages robustly activated the ISR in comparison to M0- and M2-like CM, as shown by increased eIF2α phosphorylation and ATF4 accumulation by immunoblotting and their densitometric quantification (Fig. 2B-D**)**. Consistently, confocal immunofluorescence showed a marked nuclear enrichment of ATF4 in cells exposed to M1-like CM, compared with M0 or M2-like CM (Fig. 2E), and quantification confirmed a significant increase in nuclear ATF4 under this condition (Fig. 2F). Extending these observations across TNBC models with distinct driver alterations [39], M1-like CM consistently induced selective ISR activation in BT-549 (Fig. S3A-D) and SUM159 cells (Fig. S3E-H), as detected by immunoblotting and ATF4 nuclear accumulation, supporting a macrophage-driven and cell-line independent mechanism.

To determine whether this response was intrinsically restricted to TNBC cells, we extended the analysis to the ER-positive MCF7 and BT-474 models. In both cell lines, M1-like CM increased ATF4 abundance and nuclear accumulation relative to M0- and M2-like CM, with associated eIF2α phosphorylation (Fig. S3I-P). Thus, despite the lower enrichment of ISR programs in patient-derived ER-positive tumors relative to TNBC, these cells retain the capacity to activate the ISR in response to inflammatory macrophage-derived signals.

We next extended CM exposure to 7 days to test the persistence of response. ATF4 accumulation and nuclear enrichment remained evident after prolonged M1-like CM exposure, supporting the stability of the inflammatory macrophage-induced cellular state, whereas phopho-eIF2α levels were variable at this later time point (Fig. 2G-K), consistent with the established negative feedback attenuation of ISR signaling [40].

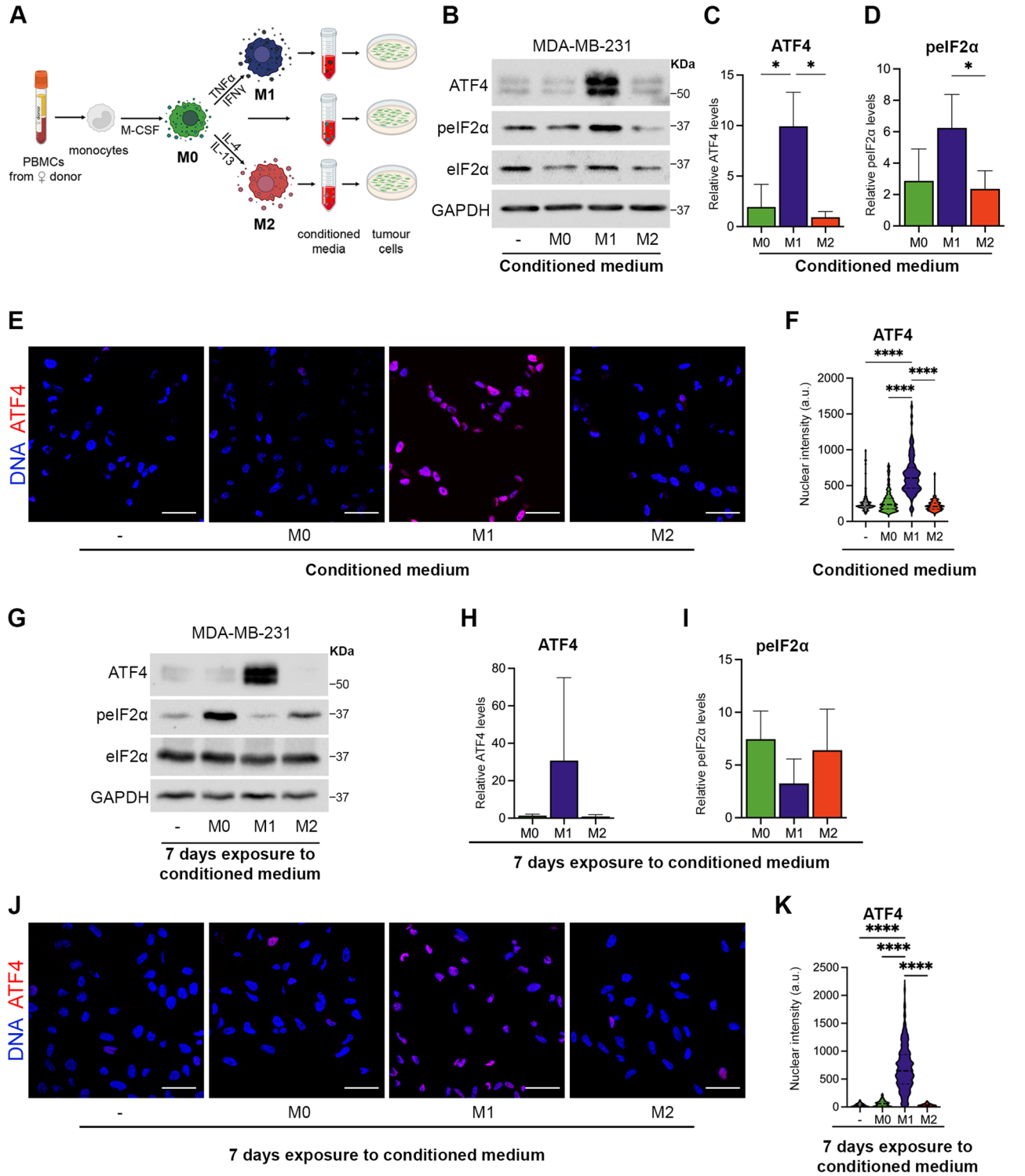

Fig. 2 M1-like macrophage secretome induces acute and persistent ISR activation in TNBC cells. **A** Experimental workflow: Monocytes were isolated from pooled PBMCs of female donors and differentiated into macrophages with M-CSF (20 ng/ml) for 5 days. Macrophages were then polarized for 48 h with TNF-α (100 ng/ml) + IFN-γ (20 ng/ml) to generate M1-like macrophages; IL-4 (40 ng/ml) + IL-13 (20 ng/ml) to generate M2-like macrophages; or maintained with M-CSF to obtain naïve M0 macrophages. After polarization, cells were washed, fresh medium was added, and conditioned medium (CM) was collected 24 h later and administered to tumor cells for 48 h. **B** Representative Western Blot of ISR activation in MDA-MB-231 cells following exposure to macrophage CM for 48 h, showing ATF4 protein levels and eIF2α phosphorylation relative to control (fresh medium). **C-D** Densitometric quantification of (**C**) ATF4 and (**D**) phosphorylated eIF2α to total eIF2α ratio in MDA-MB-231 cells treated with CM from differentially polarized macrophages, normalized to control. Data represent mean ± SD of ≥ 3 biological replicates. Statistical analysis: Kruskal-Wallis test. **E** Representative confocal immunofluorescence images of MDA-MB-231 cells treated with macrophage CM for 48 h. Nuclei (Hoechst 33342, blue) and ATF4 (red) are shown. Scale bars, 50 µm. **F** ATF4 quantification: ATF4 fluorescence intensity within the Hoechst-masked nuclear region was measured per single cell. **G** Representative Western Blot after 7 days of CM exposure. **H-I** Densitometric quantification of (**H**) ATF4 and (**I**) phospho-eIF2α/total eIF2α after 7 days. **J** Representative confocal images after 7 days of CM exposure. DNA, blue; ATF4, red. Scale bars, 50 µm. **K** Single-cell nuclear ATF4 intensity after 7 days. All data represent ≥ 3 biological

Collectively, these results show that soluble factors released by pro-inflammatory macrophages preferentially engage the ISR across breast cancer models. The patient-derived co-enrichment of ISR and inflammatory macrophage programs identifies TNBC as the biological and clinical context in which the relevance of this signaling circuit is most strongly supported. Accordingly, we focused our subsequent mechanistic and functional analyses on TNBC models.

Pro-inflammatory macrophage secretome drives ISR-dependent 3D invasion

Given the established link between ISR activation and pro-metastatic traits in cancer cells, we next asked which phenotypic consequences accompany M1-like macrophage-induced ISR activation in TNBC cells.

M1-like CM caused a modest increase in caspase 3/7 positivity (Fig S4A) and induced a mild G1 accumulation with a corresponding reduction in S phase (Fig. S4B), indicating that pro-inflammatory macrophage-derived signals affect both survival and cell cycle progression. However, these effects were not substantially reversed by ISR inhibition via 2BAct (Fig S4C-D), suggesting that apoptosis and G1 delay are not major ISR-dependent outputs of the M1-like secretome signaling cascade. The effects of macrophage-derived CM on proliferation and cell death were orthogonally confirmed via both EdU incorporation (Fig. S4E-F) and longitudinal label-free live-cell imaging with Nanolive (Fig. S4G-H), whereby M1-like CM was associated with trends toward reduced proliferation and increased apoptotic events. However, these trends were not specific to M1-like CM, as comparable effects were observed with M0- and M2-like CM.

We therefore focused on invasion as candidate aggressive phenotype downstream M1-like macrophage induced ISR activation. To investigate mechanisms potentially contributing to tumor-cell migration, we examined factors involved in extracellular matrix remodeling. MMP9 mRNA expression was significantly increased following M1-like CM treatment (Fig. S4I), suggesting enhanced matrix-remodeling activity associated with TNBC invasion [41].

These observations prompted us to test directly whether M1-like macrophage-induced ISR activation translates into enhanced invasive behavior in a physiologically relevant 3D setting. To this end, we employed a standardized microfluidic chip-based invasion assay in which MDA-MB-231 cells were seeded adjacent to a 3D collagen type I matrix under a controlled serum gradient, enabling highly reproducible, real-time, quantitative single-cell tracking in a physiologically relevant extracellular matrix setting (Fig. 3A). Relative to unconditioned medium, CM from M0 or M2-like macrophages modestly reduced invasion, whereas, strikingly, M1-like CM markedly increased both the number of invading cells (Fig. 3B-C) and the migration distance within the matrix (Fig. 3D), indicating acquisition of a more invasive phenotype. These results show that soluble factors released by pro-inflammatory macrophages are sufficient to enhance invasion in a physiomimetic 3D microenvironment, consistent with a functional link between M1-like macrophages-driven stress signaling and metastatic competence.

To test whether the increased invasiveness was depended on ISR activation, we inhibited the pathway using two complementary strategies. Pharmacological ISR blockade with 2BAct, a small molecule that prevents inhibition of eIF2B by phosphorylated eIF2α, reduced M1-like CM-induced ISR activation, as shown by reduced ATF4 accumulation (Fig. 3E) and markedly reduced invasion compared to vehicle-treated controls (Fig. 3F-H). Similarly, expression of a dominant-negative, non-phosphorylatable eIF2α mutant (S52A) prevented ATF4 induction in response to M1-like CM (Fig. 3I) and strongly reduced both the number of invading cells and migration distance under M1-like CM conditions (Fig. 3J-L).

This body of evidence identifies invasion as a principal functional consequence of macrophage-induced ISR activation and shows that pro-inflammatory macrophage-derived factors couple stress signaling to metastatic behavior in a physiomimetic 3D microenvironment.

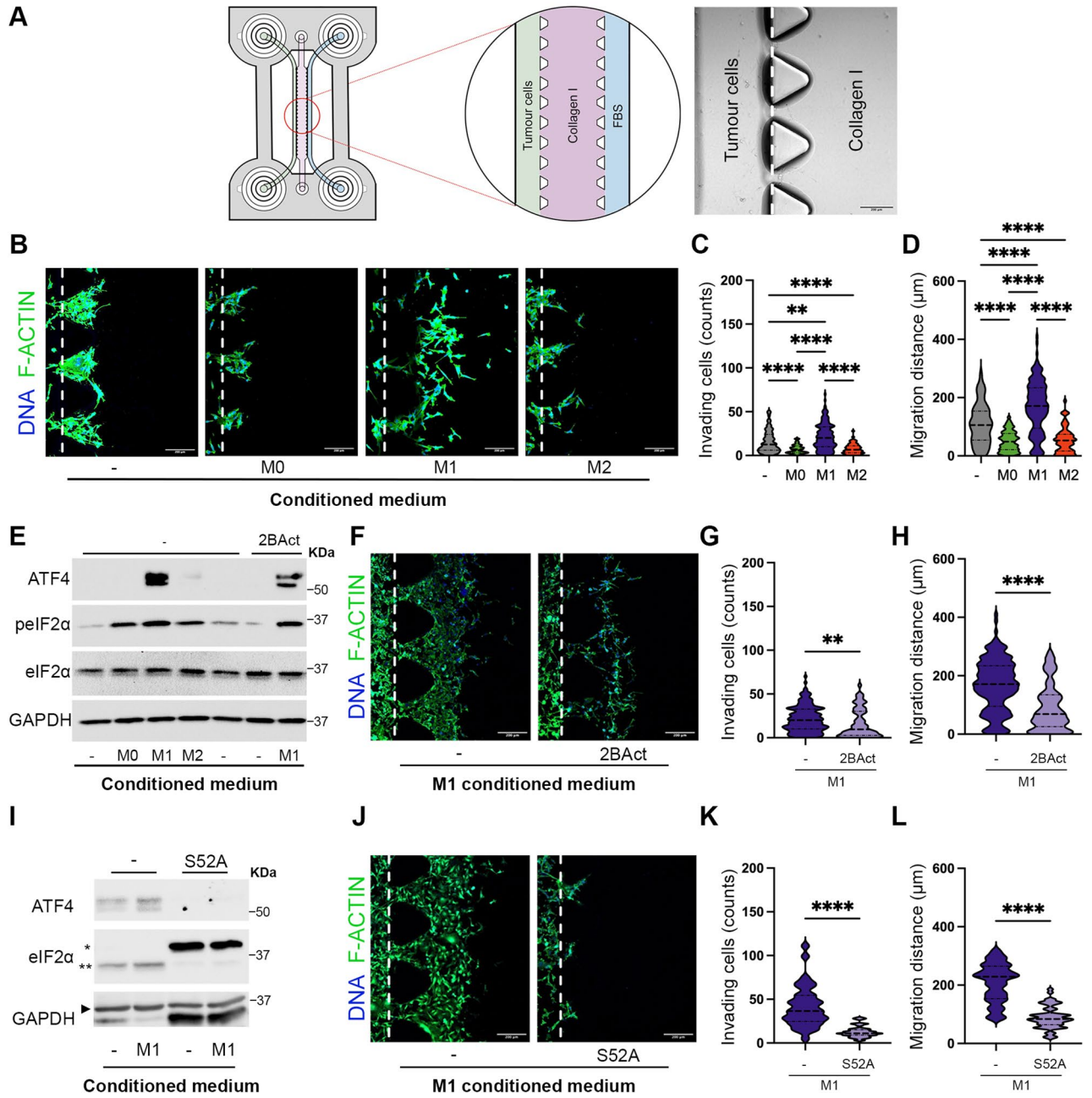

Fig. 3 The pro-invasive effect of the M1-like macrophage secretome on TNBC cells is ISR-dependent. **A** Schematic of the invasion assay in the idenTx 3 microfluidic device: MDA-MB-231 cells were seeded in the left chamber (green) and induced to migrate toward 20% FBS-containing medium in the right chamber (light blue) across a central collagen I channel (3 mg/ml; pink). Representative brightfield image showing the collagen I channel edge (white dashed line). **B** Representative confocal images of the invasion assay: Z-projection of cells invading the collagen I channel after 48 h treatment with CM from differentially polarized macrophages, compared with control. F-Actin was stained with phalloidin (green), and nuclei with propidium iodide (blue). The collagen I channel edge is indicated by a white dashed line. Scale bars, 200 µm. **C-D** Quantification of invasion. **C** Invading cells were quantified by counting nuclei within the collagen I channel. **D** Invasion depth was calculated as the distance from the collagen I channel edge to each cell nucleus. Data represent 8 independent biological replicates. Statistical analysis: Kruskal-Wallis test. **E** Representative Western Blot showing reduced ISR activation upon pharmacological inhibition with 2BAct (100 nM) in the presence of M1 conditioned medium (M1-CM). MDA-MB-231cells were treated for 48 h with CM from differentially polarized macrophages (as indicated) and with vehicle (DMSO), 2BAct alone, or 2BAct+M1-CM. eIF2α phosphorylation and ATF4 protein levels are shown. **F** Representative confocal images (Z-projection) of MDA-MB-231 cells invading a collagen I channel after 48 h treatment with M1-CM±2BAct, compared to the indicated controls. F-actin (phalloidin, green) and nuclei (PI, blue) are shown; the collagen channel edge is indicated by a white dashed line. Scale bars, 200 µm. **G-H** Quantification of invasion upon ISR pharmacological inhibition. **G** Invading cells were quantified by counting nuclei within the collagen I channel. **H** Invasion depth was calculated as the distance from the collagen I channel edge to each cell nucleus. Data represent three independent biological replicates. Statistical analysis: Mann-Whitney test. **I** Representative Western Blot showing impaired ISR activation in eIF2α S52A-expressing MDA-MB-231 cells (non-phosphorylatable) upon exposure to M1-CM for 48 h compared to control. eIF2α phosphorylation and ATF4 are shown. Single asterisk represents exogenous protein, double asterisk represents endogenous protein, arrow-

CXCL10 links inflammatory macrophage mediators to ISR activation and invasion in TNBC

To identify the soluble mediators within the M1-like secretome responsible for ISR activation and the associated invasive phenotype in TNBC cells, we profiled 105 cytokines and chemokines using a proteome profiler array. Comparative analysis highlighted IFN-γ-induced chemokines, most prominently CXCL9 and CXCL10, together with IFN-γ itself, among the most enriched components of M1-like CM relative to the other macrophage conditions (Fig. 4A; Fig. S5A). We prioritized CXCL10 for further studies (Fig. 4B), based on its reported role in macrophage-tumor cell crosstalk, its elevated expression in TNBC-associated macrophages, and emerging links between CXCL10 signaling and stress response pathways [42], which together positioned it as a plausible novel mediator of the inflammatory macrophage-ISR-invasion axis explored here.

Recombinant CXCL10 alone was sufficient to activate the ISR in TNBC cells, as shown by dose-dependent increase in eIF2α phosphorylation and ATF4 accumulation that reached a plateau at low nanomolar concentrations (Fig. 4C). Functionally, CXCL10 alone was also sufficient to promote TNBC cells invasion in the microfluidic 3D assay (Fig. 4D), with significant gains in both the number of invading cells and the migration distance compared to untreated controls (Fig. E-F). Thus, a single M1-enriched chemokine was sufficient to recapitulate both the stress-signaling and pro-invasive effect of the pro-inflammatory macrophage secretome.

To directly test the contribution of CXCL10 to M1-like CM-induced ISR activation, we pre-incubated M1-like CM with a neutralizing anti-CXCL10 antibody. CXCL10 blockade markedly reduced ATF4 amount and nuclear accumulation in TNBC cells (Fig. 4G, Fig S5B), indicating attenuation of M1-like CM-induced ISR activation. Importantly, neutralization of CXCL10 also blunted the pro-invasive effect of M1-like CM in the 3D invasion assay, as shown in (Fig. 4I) and quantified for both invading cell number and migration distance (Fig. 4J-K).

Together, these results identify CXCL10 as a key effector of the pro-inflammatory macrophage secretome that is sufficient to induce ISR signaling and invasion and substantially contributes to the ability of M1-like macrophage-derived factors to couple inflammatory signaling to ISR-dependent metastatic behavior in TNBC cells.

CXCR3 couples CXCL10 to ISR-linked 3D invasion in TNBC

Given that CXCR3 is the canonical receptor for CXCL10 and related IFNγ-inducible chemokines enriched in the M1-like secretome [43], we investigated whether it serves as the tumor-cell gateway through which pro-inflammatory macrophage mediators engage the ISR and promote invasion in TNBC. Importantly, defining this interface is also translationally relevant, as it may reveal an actionable node for tumor-targeted intervention within the macrophage-tumor signaling axis.

CXCR3 knockdown markedly reduced ATF4 levels in TNBC, both under basal conditions and following stimulation with M1-like CM (Fig. 5A), identifying CXCR3 as a key upstream mediator of macrophage-induced stress signaling and suggesting that CXCR3-dependend inputs from the microenvironment may also contribute to a basal ISR activity.

We next tested whether CXCR3 was required for the pro-invasive effects of the M1-like secretome in the microfluidic 3D invasion assay (Fig. 5B). As observed previously, M1-like CM increased the number of invading cells and the migration distance within the collagen matrix. Strikingly, CXCR3 knockdown completely abrogated the increase in invading cell number induced by M1-like CM, restoring invasion counts to basal level (Fig. 5C). This identifies CXCR3 as a critical determinant of the entry of TNBC cells into the invasive program triggered by pro-inflammatory macrophage mediators. By contrast, although CXCR3 knockdown abrogated ISR activation and strongly reduced the number of cells entering the matrix, the smaller fraction that still invaded travelled farther than the untreated siCTRL, irrespective of M1-like CM (Fig. 5D). This suggests that the CXCR3-ISR axis primarily controls invasion entry, whereas migration within the matrix can persist through CXCR3-independent mechanisms.

To assess the clinical relevance of this axis, we returned to TCGA-BRCA ad found that CXCR3 expression was elevated not only in TNBC but also in HER2+tumors relative to ER/PR+ tumors (Fig. 5E), extending this

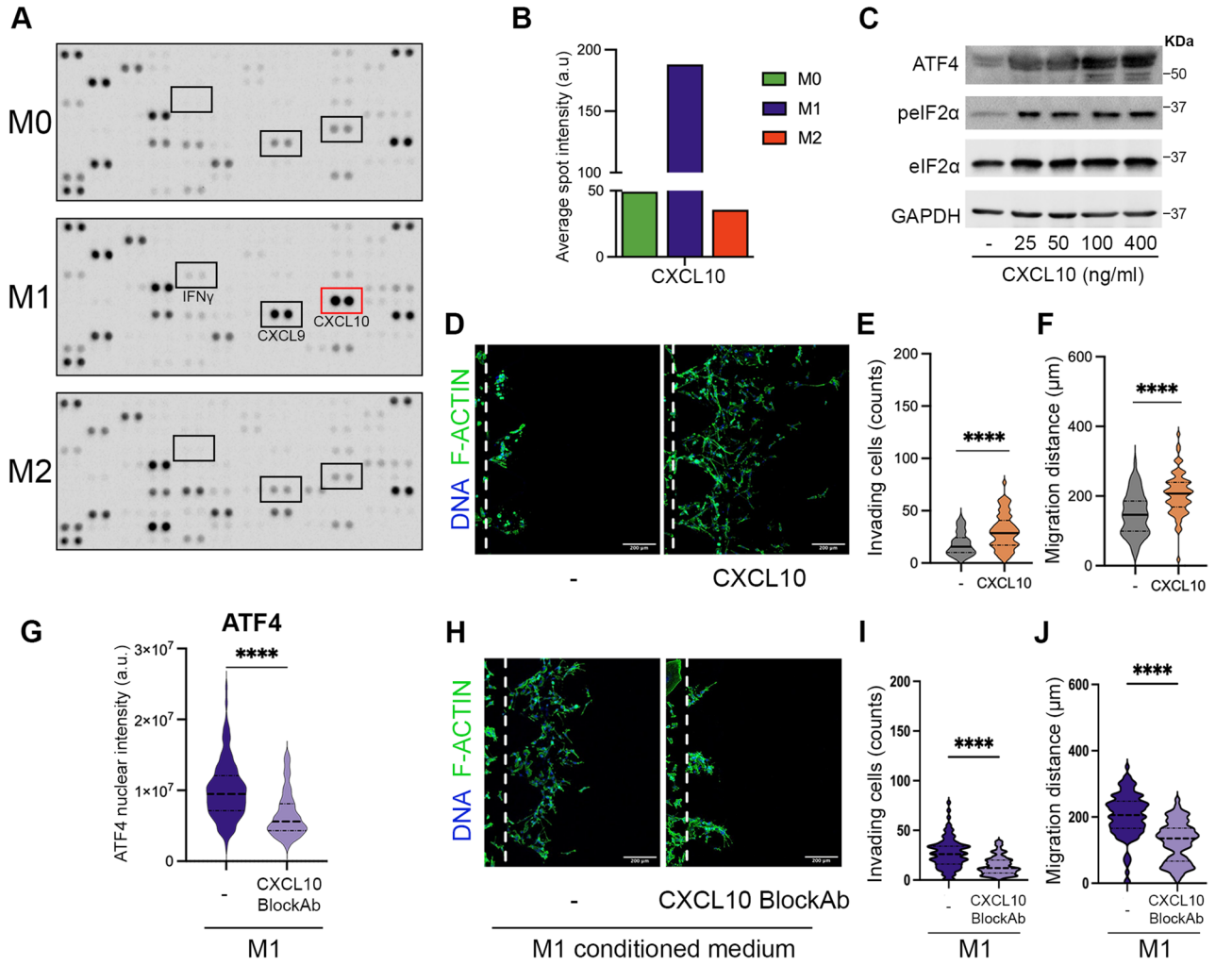

Fig. 4 CXCL10 is enriched in the M1-like macrophage secretome and drives ISR activation and invasion in TNBC cells. **A** Proteome Profile human XL Cytokine Array showing the detection of the cytokines panel after incubation with M0, M1-like and M2-like macrophages CM. In the panel are evidenced the areas corresponding to IFNγ, CXCL9 and CXCL10. **B** CXCL10 levels in CM from M0, M1-line and M2-like macrophages, measured with the Proteome Profiler human XL Cytokine Array Kit. **C** Dose-response immunoblot showing ISR activation in MDA-MB-231 cells treated with recombinant CXCL10 (25–400 ng/ml) assessing ATF4 and eIF2α phosphorylation. **D** Representative confocal images (Z-projection) from the idenTx 3 microfluidic invasion assay showing MDA-MB-231 invasion into a collagen I channel in the absence or presence of CXCL10 for 48 h. F-actin (phalloidin, green) and nuclei (PI, blue) are shown; the collagen channel edge is indicated by a white dashed line. Scale bars, 200 μm. **E-F** Quantification of invasion in (**D**): (**E**) invading cells quantified by counting nuclei within the collagen I channel. **F** Invasion depth calculated as the distance from the collagen I channel edge to each cell nucleus. Data represent three independent biological replicates. Statistical analysis: Mann-Whitney test. **G** Quantification of nuclear ATF4 in immunofluorescence of MDA-MB-231 cells treated with M1-CM in the absence or presence of a CXCL10 blocking antibody (CXCL10 BlockAb), measured as ATF4 fluorescence within the Hoechst-defined nuclear region. Data represent three independent biological replicates. Statistical analysis: Mann-Whitney test. **H** Representative confocal images (Z-projections) from the microfluidic invasion assay showing MDA-MB-231 invasion in response to M1-CM with or without CXCL10 BlockAb. (DNA blue, F-actin green). **I-J** Quantification of invasion in (**H**): (**I**) invading cells quantified by counting nuclei within the collagen I channel. **J** Invasion depth calculated as the distance from the collagen I channel edge to each cell nucleus. Data represent three independent biological replicates. Statistical analysis: Mann-Whitney test

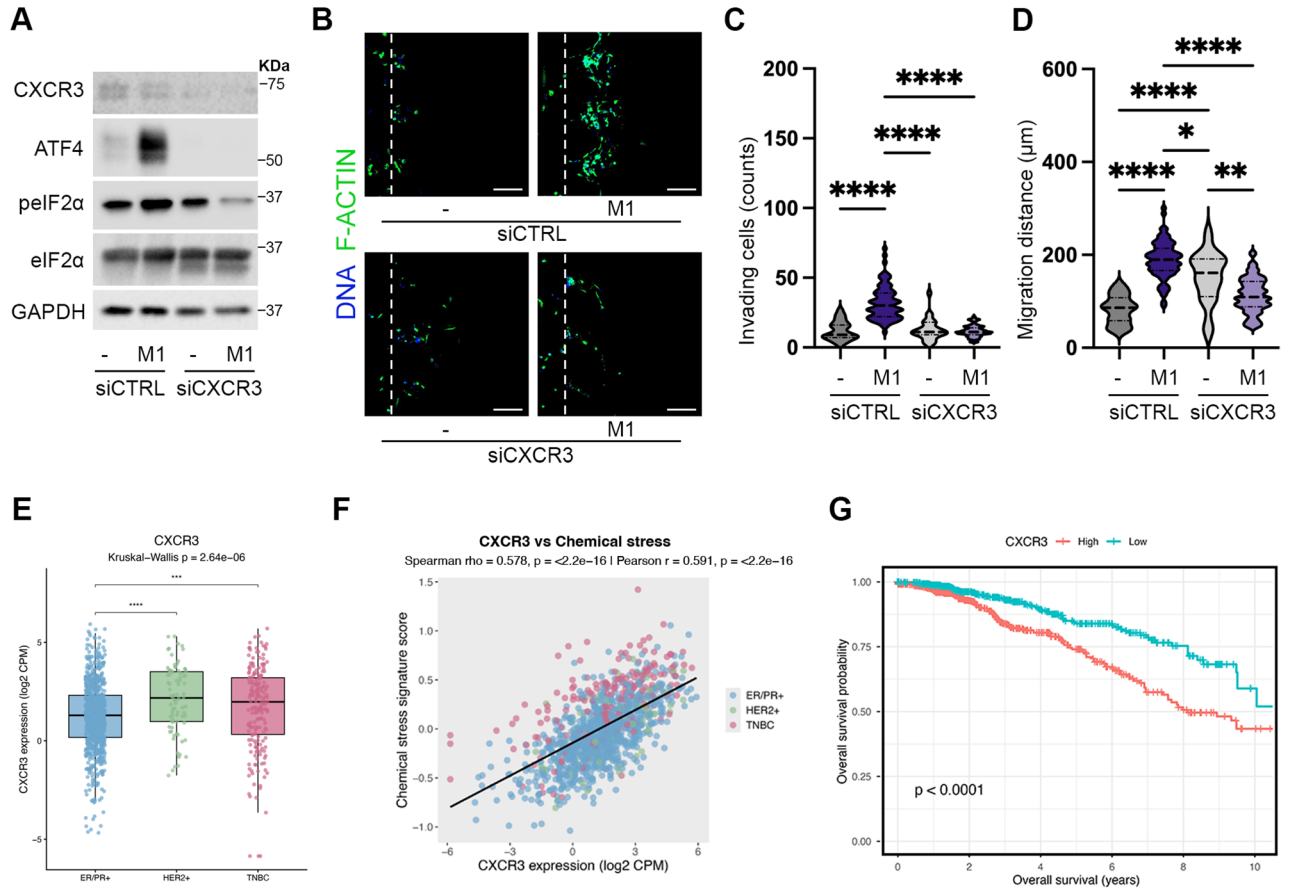

Fig. 5 CXCR3 couples M1-like secretome-induced ISR activation and 3D invasion in TNBC. **A** Representative immunoblot of ISR activation in siCTRL and siCXCR3 MDA-MB-231 cells untreated or exposed to M1-like CM, showing efficiency of CXCR3 knockdown, and phopsho-eIF2α and ATF4 levels. **B** Representative images (Z-projection) from the idenTx 3 microfluidic invasion assay showing MDA-MB-231 cells transfected with siCTRL or siCXCR3 and exposed to the indicated conditions. F-actin (phalloidin, green) and nuclei (PI, blue) are shown; the collagen channel edge is indicated by a white dashed line. Scale bars, 200 µm. **C-D** Quantification of invasion in (**B**): (**C**) invading cells quantified by counting nuclei within the collagen I channel. **D** Invasion depth calculated as the distance from the collagen I channel edge to each cell nucleus. Data represent three independent biological replicates. Statistical analysis: Kruskal-Wallis test. **E** Boxplot representing CXCR3 expression across TCGA-BRCA molecular subtypes. **F** Correlation between CXCR3 expression and the chemical stress signature score across TCGA-BRCA tumors. **G** Kaplan-Meier overall survival analysis of TCGA-BRCA patients stratified by CXCR3 expression

inflammatory-stress signaling framework to another aggressive BC subtype. Moreover, CXCR3 expression was strongly associated with the chemical stress signature (Fig. 5F), and high CXCR3 expression could predict worse overall survival probability in BC patients (Fig. 5G).

Collectively, these findings identify CXCR3 as a central mediator of the pro-inflammatory macrophage-tumor signaling circuit that couples inflammatory factors to ISR activation and metastatic competence in aggressive BC, extending this axis from mechanism to clinical relevance.

Tumor cell-intrinsic ISR signaling promotes metastatic competence in vivo

To determine whether ISR activity within TNBC cells directly contributes to metastatic potential in vivo, we generated 4T1 cells expressing a non-phosphorylatable eIF2α mutant (S52A), together with eIF2α WT and empty-vector Venus- controls, thereby establishing a "non-stressable" cell line unable to activate canonical ISR signaling

despite exposure to stress stimuli. 1×10^4 cells were orthotopically implanted into the mammary fat pad of 12 weeks-old female syngeneic BALB/c immunocompetent mice, allowing tumor progression to be assessed within an intact immune microenvironment. Primary tumor growth was monitored longitudinally, and pulmonary metastatic burden was quantified at endpoint. eIF2α S52A tumors grew modestly faster than either control group (Fig. 6A), consistent with release from an ISR-dependent proliferative restraint in rapidly expanding tumors [44]. In marked contrast, disruption of eIF2α phosphorylation markedly impaired metastatic dissemination: despite their larger primary tumor mass, eIF2α S52A tumors generated substantially fewer lung metastases with a decreased mass, providing a significantly reduced metastatic burden compared to either eIF2α WT or Venus controls (Fig. 6B-D). Representative images of lungs collected at sacrifice further supported this phenotype, showing an evident reduction in the number and size of metastatic lesions in the eIF2α S52A group (Fig. 6E). Importantly, the same overall trend was reproduced in an independent second cohort of mice ($n = 5$ per condition) (Fig S6A), in which absolute metastatic counts were lower across all groups, precluding pooling of the datasets. Nevertheless, the concordant behavior observed across independent in vivo experiments strengthens the conclusion that tumor cell-intrinsic impairment of eIF2α phosphorylation reduces metastatic competence.

To determine whether eIF2α phosphorylation continued to regulate ATF4 in established metastases, we performed immunohistochemical analysis of ATF4 in lung lesions. Nuclear ATF4 positivity was reduced in the few residual metastases generated by eIF2α S52A cells relative to both control groups (Fig. 6F-G), showing that the dependence of ATF4 accumulation on eIF2α phosphorylation is retained during metastatic colonization. The low levels of ATF4 observed in mutant lesions may reflect eIF2α-independent translational control, including mTORC1/4E-BP-dependent regulation [45].

Notably, exploratory profiling of the primary tumor immune infiltrate suggested a modest reduction in M1-like macrophages in the eIF2α S52A group (Fig S6B). Remarkably, multiplex immunofluorescence staining for F4/80 and CXCL10 further revealed abundant F4/80-positive macrophages within and surrounding control metastatic foci, with CXCL10 expression detected in a subset cells (Fig. S6C). In contrast, both F4/80-positive macrophage infiltration and CXCL10 expression were substantially attenuated in the residual eIF2α S52A metastatic foci compared to control groups. These observations provide spatial support for CXCL10-expressing macrophages also in the metastatic niche and raise the possibility that tumor cell ISR activity may contribute not only to the metastatic fitness of cancer cells, but also to the maintenance of an inflammatory microenvironment enriched in the macrophage population that reinforces stress signaling.

CXCR3-positive metastatic states are associated with ISR activity

Having established CXCR3 as a mediator of macrophage-induced ISR activation and invasion in vitro, we next examined whether CXCR3 expression was associated with ISR activity in independent transcriptomic datasets derived from in vivo models of metastatic progression. We first analyzed GSE121945, a subseries of GSE121947 comprising three biological replicates each of FACS-isolated CXCR3-negative and CXCR3-positive SUM-LM1 metastatic TNBC cells [46]. CXCR3-positive cells exhibited higher ATF4 and CXCL10 expression and Chemical Stress scores (Fig. 7A) and were enriched for several ISR-related signatures, including the manually curated ISR Core 19 signature, the published ATF4 Consensus 41 signature [47], and our Chemical Stress signature, whereas the Metabolic Stress signature showed no significant enrichment (Fig. 7B and Supplementary Table 1).

We then analyzed GSE241165 single-cell RNA-sequencing data from 4T1 cells spanning primary tumor growth and bone metastatic colonization [48]. The association between CXCR3 expression and two independent measures of ISR activity, the ISR Core and Metabolic Stress signatures, became progressively stronger during metastatic progression (Fig. 7C). Together, these independent datasets link CXCR3-positive metastatic states to increased ISR activity during tumor progression.

Altogether, these findings provide direct genetic evidence that tumor-cell-intrinsic eIF2α phosphorylation promotes metastatic competence in TNBC in vivo and, together with the tissue-level and transcriptomic associations,

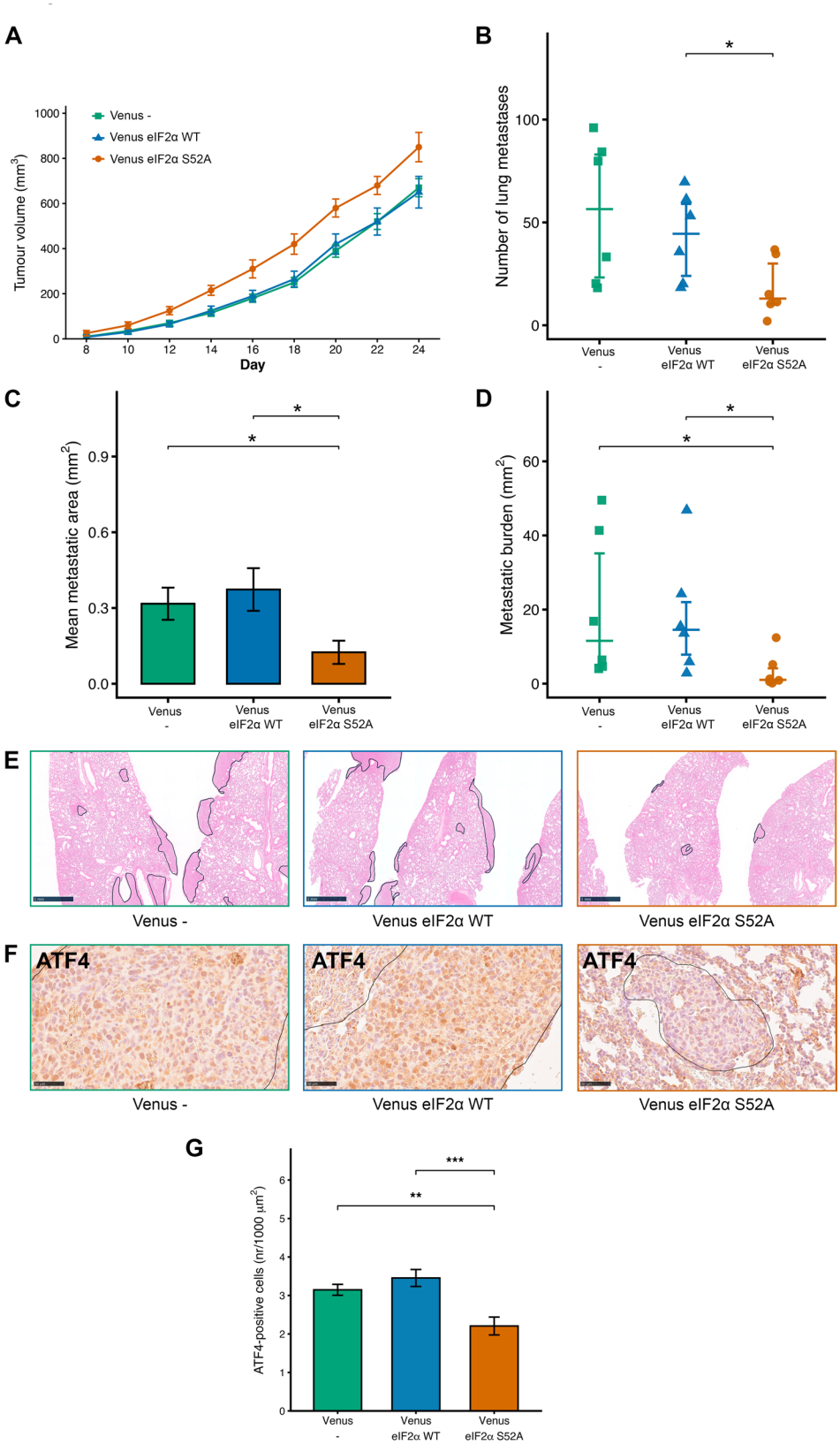

Fig. 6 Genetic disruption of eIF2α phosphorylation uncouples tumor growth from metastatic output in vivo. **A** Growth kinetics of orthotopic primary tumors formed by 4T1 Venus -, Venus eIF2α WT, or Venus eIF2α S52A cells in BALB/c syngeneic mice. **B-D** Quantification of lung metastases number (**B**), mean metastatic area (**C**), and metastatic burden (**D**) at endpoint. For (**B**) and (**D**), each dot represents one mouse; horizontal lines indicate the median and SEM. In (**C**), bars represent the mean area of metastatic lesions per group. Mann-Whitney test *p* values are indicated. **E** Representative images of Haematoxylin & Eosin (H&E) staining of lungs from the indicated groups at sacrifice. Metastatic lesions are outlined in black, illustrating a reduced metastatic burden in the eIF2α S52A condition. Scale bars, 1 mm. **F** Representative images of immunohistochemical staining for ATF4 in lung sections from the indicated groups; metastatic lesion boundaries are outlined by black lines. Scale bars, 100 µm. **G** ATF4 positivity normalized to the metastatic surface area. Bars represent mean ± SEM; pairwise Mann-Whitney tests, $^{**}P < 0.01$ and $^{***}P < 0.001$

https://doi.org/10.1186/s13046-026-03821-4

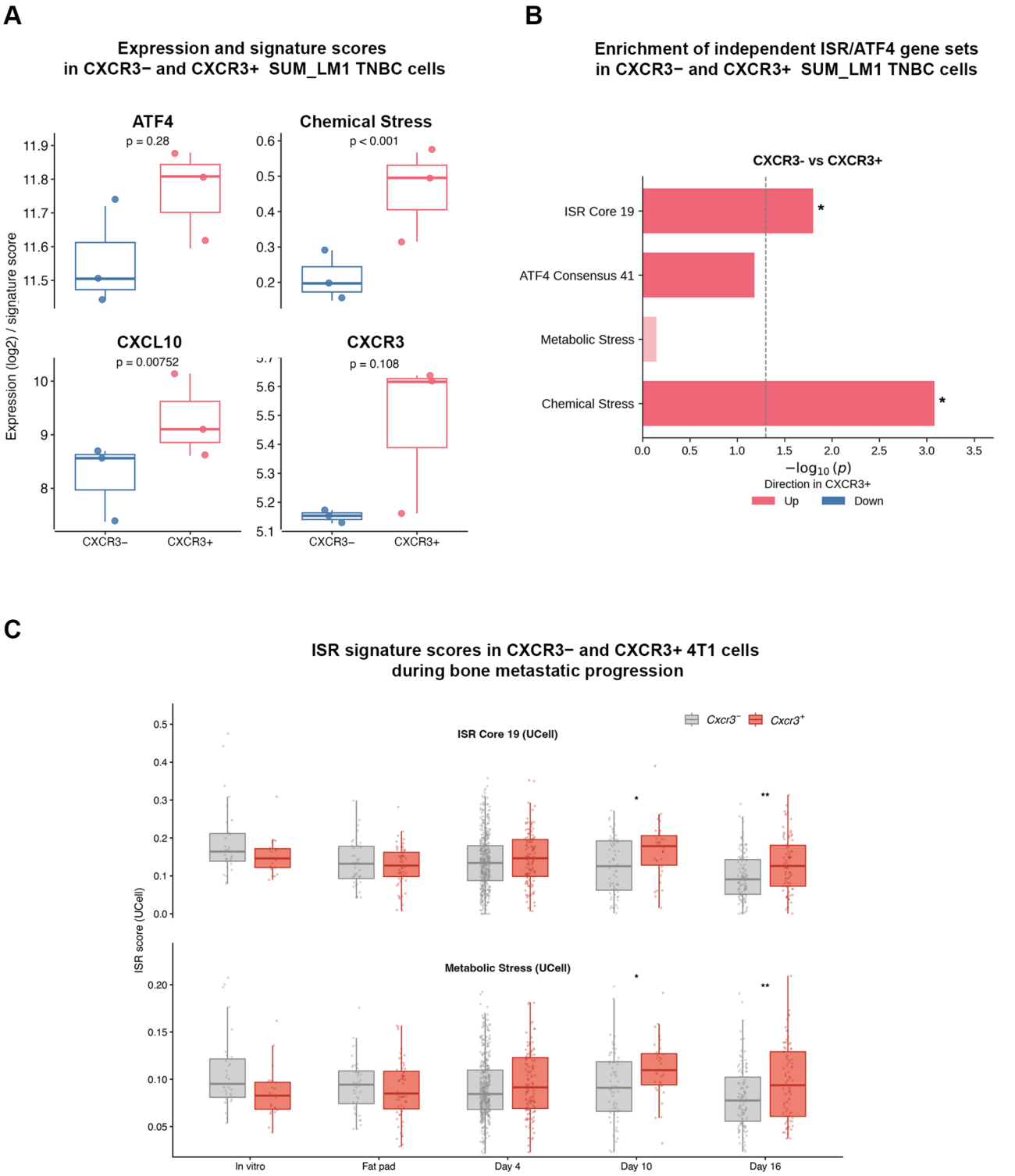

Fig. 7 CXCR3 expression is associated with ISR-related transcriptional activity during metastatic progression. **A**-**B** Analysis of GSE121945, a subseries of GSE121947, comparing FACS-isolated CXCR3- and CXCR3+ SUM-LM1 metastatic TNBC cells. **A** ATF4, CXCL10 and CXCR3 expression and Chemical Stress signature scores in CXCR3- and CXCR3+ cells. Points represent independent biological samples; box plots show the median and interquartile range. The indicated p values were calculated using paired limma moderated t-test. **B** Enrichment analysis of independent ISR- and ATF4-related gene sets in CXCR3+ relative to CXCR3- cells. Bar length represents $-\log_{10}$ (P), and color indicates the direction of enrichment in CXCR3+ cells. The dashed line indicates p= 0.05. **C** Analysis of GSE241165 single-cell transcriptomic data following 4T1 cells from in vitro culture through mammary fat-pad growth and successive stages of bone metastatic colonization. ISR Core 19 and Metabolic Stress signature scores were calculated in CXCR3- and CXCR3+ tumor cells using UCell. Each point represents an individual cell; box plots show the median and interquartile range. Comparisons were performed using two-sided Wilcoxon rank-sum tests. $P < 0.05$, *; $P < 0.01$, **

place this pathway within a broader circuit linking cancer-cell stress adaptation to macrophage-associated metastatic programming.

Discussion

Metastasis may be enabled as much by the inherent properties of cancer cells, what they are, as by what the tumor microenvironment instructs them to become, through the transmission of a stress-adaptive signals that are translated into invasive behavior. Among the inputs that shape this transition, the immune microenvironment is emerging as a critical source of instructive signals capable of modulating tumor cell plasticity.

Here, we identify an immune-to-tumor signaling axis in which a soluble factor released by pro-inflammatory macrophages activates the tumor cell Integrated Stress Response, promoting invasive behavior and increasing their metastatic competence. Mechanistically, this circuit converges on CXCL10-CXCR3 signaling and identifies the ISR as a relay that decodes an inflammatory information and translates it into a pro-invasive tumor state.

The inflammatory macrophage paradox in metastatic progression

The proposed novel mechanism originates from a distinct inflammatory macrophage state the biological interpretation of which is central to understanding its tumor-promoting consequences. Although the M1-M2 dichotomy is now recognized as a simplification of macrophage biology, it remains a useful keystone for interpreting functionally distinct inflammatory states, particularly in experimentally controlled model systems designed to isolate discrete signaling mediators [49, 50].

In line with our polarization strategy, IFNγ and TNFα have been shown to drive a CXCL10-high inflammatory macrophage state [51], and their cooperation can synergistically enhance CXCL10 production through STAT1- and NF-kB-associated programs [52]. In tumors, macrophages are increasingly recognized as major producers of CXCR3 ligands, including CXCL9 and CXCL10 [53], and recent single-cell studies in breast cancer and TNBC have identified IFN-enriched CXCL10+/CXCL11 + TAM populations [54]. These observations support the biological plausibility of the macrophage state modeled here and place our findings within a broader context in which inflammatory macrophage programs, while classically linked to anti-tumor immunity, may also generate signals that cancer cells can exploit for malignant progression. Therefore, our findings highlight an important paradox: inflammatory “anti-tumor” immune states may still promote metastasis when the signals they generate are efficiently relayed within the malignant compartment. In keeping this view, the broader CXCL9/10/11-CXCR3 literature already points to a functional duality: while this axis supports immune cell trafficking, Th1 polarization and cytotoxic anti-tumor responses, the same ligands can also be hijacked by tumor cells through autocrine or paracrine signaling to promote progression and metastasis [55–57]. Therefore, our results broaden and refine the identity classically assigned to IFNγ and TNFα-stimulated macrophages and fill an important mechanistic gap by demonstrating that ISR is the signaling pathway responsible for hijacking the CXCL10-CXCR3 axis to promote metastatic invasion.

However, our findings should not be interpreted as establishing absolute specificity for the M1-like state. Indeed, TAMs occupy a continuum shaped by tumor-derived signals, including tumor-derived factors, LIF, IL-6, and IL-10, which can generate distinct TAM states and immunoregulatory programs [58–61]. Given this heterogeneity, other TAM states, or different combinations, concentrations, and temporal sequences of TAMs-derived stimuli, could also engage the ISR and promote aggressive tumor-cell phenotypes. Future research will be needed to define the broader spectrum of TAM states capable of engaging the ISR and their contribution to cancer progression.

The induction of ISR by M1-like CM in MCF7 and BT-474 cells also indicates that this signaling response is not intrinsically restricted to TNBC. However, these observations establish pathway competence more than functional relevance across BC subtypes. Patient-derived analyses identify TNBC as the subtype in which ISR

activity and inflammatory macrophage programs most strongly converge. This interpretation is consistent with subtype-dependent macrophage-tumor cell interactions and the association of macrophages with TNBC metastatic progression and outcome [23, 62, 63].

ISR as a relay of inflammatory stress signal

Defining the ISR as the tumor cell relay of macrophage-derived inflammatory signaling provides a broader rationale for understanding its contribution to metastatic potential. In cancer, the ISR is increasingly recognized as an adaptive pathway that integrates a plethora of intracellular and extracellular stresses into a common translational response, with context-dependent consequences for tumor cell survival, phenotype switching and metastatic progression [9, 64–66].

The correlation and subtype enrichment analyses of a plethora of microenvironmental stress signatures broaden the biological context of ISR activation and support its association with multiple stress programs relevant to TNBC, and interestingly the divergent behavior of the acidic pH signature indicates that this convergence is stress-selective and not universal.

Within this broad view, our findings identify M1-like macrophage-derived CXCL10 as a previously unrecognized extracellular trigger of ISR activation in TNBC cells and position the ISR as the intracellular machinery at the crossroad between inflammatory microenvironmental signaling and tumor cell invasive potential. This model provides a rationale for how inflammatory stress can enhance metastatic fitness [67]. Indeed, the role of ISR is intrinsically pleiotropic [10]: depending on the intensity, duration and cellular context of eIF2α phosphorylation, it can either sustain survival and plasticity or promote cell death. Therefore, in cancer, stress can act both as a challenge and as selective pressure. Cells that survive through stress are those able to exploit ISR-dependent translational and transcriptional reprogramming to maintain plasticity and acquire an aggressive phenotype [68].

The prolonged exposure experiment provides temporal support to this model: ATF4 accumulation remained evident after 7 days of M1-like CM despite decreased phospho-eIF2α levels, consistent with persistence of the downstream ISR program following feedback-mediated attenuation of the ISR signaling cascade [40]. This temporal dissociation suggests that macrophage-derived stress signals can produce adaptive effects that have lasting effects. In this view, our data suggest that macrophage-derived inflammatory mediators both challenge TNBC cells and create a selective pressure that favors cells capable of hijacking the adaptive ISR programs to convert the stress into invasive behavior.

The EMT Hallmark enrichment should be interpreted within the broader framework of epithelial–mesenchymal plasticity, which includes dynamic changes in tumor cell motility, invasiveness, and interaction with the extracellular matrix and not a binary phenotypic transition [69, 70]. This interpretation is particularly relevant to MDA-MB-231 cells, which already exhibit predominantly mesenchymal characteristics [71, 72]. Within this context, the increased MMP9 expression induced by M1-like CM identifies a potential matrix-remodeling component of the macrophage-driven response, consistent with the established role of tumor cell-derived MMP9 in TNBC metastasis and with previous evidence linking CXCR3 ligands to MMP9 induction in MDA-MB-231 cells [41, 73].

Although our data characterize the functional ISR output in tumor cells, evidence that ISR-related pathways are also implicated in the inflammatory macrophages signaling mechanisms supports the idea that tumor cell aggressiveness may emerge within a broader stress-inflammation network. In this context, the concept of "stress propagation" acquires a particular relevance. ISR signaling is closely linked to immunity, and can promote cytokine production and local intercellular communication during inflammatory states [74, 75]. For example, ATF4 has been implicated in macrophage inflammatory functions [76] and, in some context, in M1-like polarization [77, 78]. Moreover, the contribution of the eIF2α kinase HRI to innate immune signal transduction through eIF2α-ATF4 has been demonstrated in bacterial infection [79]. Although we did not directly assess ISR activation in the polarized macrophage used in our model, these observations support the hypothesis of a macrophage-to-tumor wave of ISR-associated information.

CXCL10-CXCR3 as the mechanistic interface of inflammatory stress relay

The CXCL10-CXCR3 arm of this circuit provides a mechanistic and translational interface for our model. CXCL10 is a canonical interferon-inducible chemokine which expression is typically low at baseline and strongly induced by IFNγ, with a possible synergistic amplification by TNFα [55]. CXCL10 is produced not only by macrophages, but also by dendritic cells, fibroblasts, endothelial cells, and, in some settings, by tumor cells themselves [80]. This wider source is important for two reasons. First, it supports the physiological plausibility of our model, since the cytokine conditions used to polarize macrophages in vitro are the same as those known to drive CXCL10-rich inflammatory stares. Second, it raises the possibility that macrophages are not the only source of this signal in vivo. Future work should therefore consider whether CXCL10 represents a broader inflammatory currency through which multiple immune and stromal compartments transmit stress-related information to tumor cells. That possibility is especially attractive in TNBC, where the immune microenvironment is heterogeneous and dynamically remodeled during progression and therapy [81].

On the receiving side, CXCR3 appears to define a tumor cell state of heightened competence to interpret this message. In our data, CXCR3 expression is associated to aggressive breast cancer subtypes and correlates with an ISR-related signature, supporting the idea that CXCR3-high tumor cells are particularly prone to convert inflammatory cytokine input into the ISR-linked aggressive output, making it a gatekeeper of susceptibility to macrophage-derived instructions.

CXCR3 is expressed not only by tumor cells but also activated T cells, NKs, macrophages and dendritic cells, and its function is determined by ligand availability, isoform usage and cellular context [82, 83]. For this reason, any therapeutic proposal must be approached with caution. At the same time, breast cancer studies have shown that CXCR3 targeting can suppress tumor cell migration and metastasis while improving host anti-tumor immunity [56], suggesting that this node may be proposed as a potential hit for cancer-specific targeted therapy.

Our in vivo data strengthen this translational rationale while also defining its current limits. By using a dominant negative non-phosphorylatable eIF2α S52A model in an immunocompetent murine setting, we could test the contribution of tumor cell-intrinsic ISR to dissemination within an intact immune microenvironment. The result was appreciable: loss of eIF2α phosphorylation reduced the metastatic burden despite a slightly faster primary tumor growth, reinforcing the notion that the ISR is a tumor cell intrinsic inducer of metastatic competence. Moreover, the residual S52A lung lesions contained fewer ATF4-positive tumor cells, confirming that canonical eIF2α phosphorylation continues to regulate ATF4 accumulation during metastatic colonization. Exploratory immune profiling suggested a modest reduction in M1-like macrophages in S52A primary tumors, while F4/80-CXCL10 co-staining localized CXCL10-expressing macrophages within and around metastatic foci and showed less prominent staining in the small S52A lesions. These observations raise the possibility of a reciprocal relationship in which tumor cell ISR activity supports metastatic fitness while contributing to the maintenance of a macrophage-enriched inflammatory niche. Consistent with this model, analyses of independent metastatic datasets linked CXCR3-positive tumor cell states to increased ISR activity, with the association between CXCR3 expression and two distinct ISR signatures becoming progressively stronger during metastatic progression. Although these findings do not establish an in vivo direct causal interaction, since they do not substitute for direct resolved genetic testing of CXCL10 or CXCR3 in vivo, they provide complementary tissue-level and transcriptomic support for the proposed macrophage-CXCL10-CXCR3-ISR circuit.

Conclusions

In conclusion, our study defines an immune-to-tumor signaling circuit in which pro-inflammatory macrophages engage the tumor cell ISR to drive invasion in TNBC. These findings show that metastatic progression depends both on tumor-intrinsic programs and on the capacity of tumor cells to decode inflammatory signals from the microenvironment. By placing the ISR at the interface between macrophage-derived inflammation and tumor cell

plasticity, our work establishes a rationale for non-cell-autonomous stress adaptation in cancer. Within this framework, the CXCL10-CXCR3 axis emerges as a key mechanistic interface and a potential therapeutic target. More broadly, our data raise the possibility that stress adaptation propagates across the tumor microenvironment as a multicellular process with consequences for dissemination and tumor-immune remodeling. Defining the extent and therapeutic vulnerabilities of this circuit will be a crucial next step.

Materials and methods

Cell lines, culture conditions, and treatments

The human MDA-MB-231 (ATCC HTB-26; RRID: CVCL_0062), BT-549 (ATCC HTB-122; RRID: CVCL_1092), MCF7 (ATCC HTB-22; RRID: CVCL_0031), BT-474 (ATCC HTB-20; RRID: CVCL_0179) and 293T (ATCC CRL-3216, RRID: CVCL_0063) cell lines, as well as the murine 4T1 line (ATCC CRL-2539, RRID: CVCL_0125) were purchased from ATCC. SUM-159PT (RRID: CVCL_5423) cells were sourced from BioIVT. All cell lines were authenticated by the vendor and fortnightly tested to exclude mycoplasma contamination by PCR. Cells were maintained in RPMI 1640 supplemented with 10% heat-inactivated Fetal Bovine Serum (Thermo Fisher Scientific), GlutaMAX™ (Thermo Fisher Scientific), and 1% Penicillin-Streptomycin (10,000 U/mL) (Thermo Fisher Scientific) at 37 °C in a humidified atmosphere containing 5% CO_2. Experiments were performed using cells within 20 passages after thawing and cultured continuously no longer than three months.

Where indicated, cells were treated with conditioned media (CM) derived from M0, M1-like, or M2-like macrophages, 2BAct (37788, Cayman Chemical) or CXCL10/IP-10 (266-IP, Bio-Techne) under the experimental conditions specified for each assay. CM exposures were 48 h unless otherwise stated; prolonged-exposure experiments used 7 days of CM treatment.

Generation of non-phosphorylatable eIF2a S52A cell lines

Lentiviral infection was used to create MDA-MB-231 S52A and 4T1 cell lines stably expressing Venus-P2A-3XFLAG and Venus-P2A-eIF2a wild-type as controls, and Venus-P2A-eIF2a S52A to create dominant negative non-phosphorylatable cell lines.

Recombinant lentivirus was made in 293T producer cells using the lentiviral vector pCSII-EF-MCS [9], seeded onto poly-L-lysine-coated plates and the vectors were co-transfected with Gag/Pol/Rev- and VSV- containing vectors. The medium was refreshed after 16 h, the virus-containing supernatant was harvested 72 h after transfection and filtered through a 0.45 µm syringe filter. TNBC cells were infected by incubation with the viral suspension for 24 h. Homogenous inter-cell line and intra-cell line populations were obtained by cell sorting of Venus-positive cells using a 488 nm blue excitation laser with a 530/50 nm bandpass filter with the cell sorter BD FACSAria Fusion Flow Cytometer (BD Biosciences).

In vivo tumor growth and metastasis assessment

In vivo experiments were conducted exclusively in female mice. Six- to eight-week-old female BALB/c mice were obtained from Charles River Laboratories (Calco, Italy) and handled in accordance with European Community guidelines. All procedures were approved by the Ministry of Health (protocol number CC652.72).

Each experimental group included 6 mice in the main cohort. An independent replication cohort, analyzed separately, included 5 mice per group. Murine 4T1 cells expressing eIF2α S52A, eIF2α WT, or empty-vector Venus control were used to evaluate the role of tumor cell-intrinsic ISR signaling in vivo. Cells were resuspended in 50 µL of PBS and injected into the left mammary fat pad of syngeneic BALB/c immunocompetent mice. Primary tumor growth was monitored every two days in a blinded manner using a digital caliper. Tumor dimensions were

recorded as the maximum (D) and minimum (d) diameters, and tumor volume was calculated using the ellipsoid formula:

$$\left(4/3\pi\,(\mathrm{d}/2)^2 \times \mathrm{D}/2\right)$$

Mice were euthanized in a CO_2 chamber when tumor volume reached approximately 500 mm^3, in accordance with the maximum size permitted by the approved protocol. Throughout the study, tumor-bearing mice did not experience more than 10% body weight loss.

For the assessment of metastatic burden, lungs from 4T1 tumor-bearing mice were collected, fixed in 10% neutral buffered formalin (BioOptica), and embedded in paraffin. To enhance the detection of microscopic metastases and ensure systematic, uniform, and random sampling, lungs were sectioned transversely to the trachea into parallel 2 mm-thick slices. The position of the first cut was randomized within the first 2 mm of the lung, yielding 5–8 slices per lung.

the cut surface facing down, sectioned, and stained with hematoxylin and eosin (BioOptica). Metastatic lesions were independently evaluated by two pathologists. To quantify the number and area of lesions, the lungs were scanned with a Nanozoomer scanner (Hamamatsu) and analyzed with NDP.view2 software using the area annotation tool. Metastatic burden was quantified by calculating the total amount of cancerous tissue present in the lungs, expressed as the sum of the total area of all visible lesions. Independent in vivo cohorts were analyzed separately. Statistical analyses of tumor growth and metastatic burden were performed using pairwise Mann-Whitney tests.

Immunohistochemical and Immunofluorescence analysis of mouse-derived samples

For immunohistochemical evaluation, lung sections were deparaffinized, serially rehydrated, and subjected to antigen retrieval by microwaving in citrate buffer (pH 6.0) for 10 min. Slides were incubated with rabbit anti-ATF4 primary antibody (ab216839, Abcam) overnight at 4 °C, followed by EnVision+ System-HRP Labelled Polymer Anti-Rabbit (Dako) for 30 min. Immunoreactivity was visualized using 3,3′-diaminobenzidine tetrahydrochloride (DAB; K3468, Dako) as the chromogenic agent, followed by nuclear counterstaining with hematoxylin (CATHE-MM, Biocare Medical). Whole-slide images (2–3 lungs per group) were scanned using a NanoZoomer scanner (Hamamatsu Photonics) and analyzed with QuPath software (v0.3.2) using the positive cell detection tool. Metastatic foci were annotated, and nuclear ATF4-positive cells were counted and normalized to the metastatic surface area (expressed as number of ATF4 + cells/1000 μm^2).

For multiplex immunofluorescence, slides were deparaffinized, serially rehydrated, and subjected to antigen retrieval by microwaving in citrate buffer (pH 6.0) for 10 min. Sequential primary antibody incubations were performed using rabbit anti-F4/80 antibody (#70076, Cell Signaling) and rabbit anti-CXCL10 antibody (bs-1502R, Bioss) 1 h at room temperature. Signal detection was carried out using HRP-conjugated secondary antibodies combined with TSA Plus Cyanine 3 System (NEL744001KT, Akoya Biosciences) and TSA Plus Fluorescein System (NEL741001KT, Akoya Biosciences). An intermediate microwave stripping step in citrate buffer (pH 6.0) was performed between antibody rounds. Nuclei were counterstained with DAPI (D9542, Sigma-Aldrich), and images were acquired using a Nikon AXR NSPARC confocal microscope.

Processing and flow cytometry analysis of immune cells of mouse-derived samples

Tumors were harvested from BALB/c tumor-bearing mice following orthotopic injection of 4T1 cells into the mammary fat pad. Only tumors of comparable size were included in the analysis. Excised tissues were placed in 50 mL tubes containing 5 mL of cold, serum-free DMEM and mechanically dissociated using a scalpel until a homogeneous cell suspension was obtained. The resulting suspension was incubated in 5 mL of serum-free DMEM supplemented with 0.1 mg/mL collagenase (Sigma-Aldrich; Cat# C0130) for 1 h at 37 °C under

continuous rotation. After enzymatic digestion, samples were filtered through a 40 µm cell strainer (Falcon; Cat# 352340) to generate single-cell suspensions. Cells were then centrifuged at 476 × g for 5 min at 4 °C, washed with cold PBS, and kept on ice. Tumor-derived cells were transferred into FACS tubes and red blood cell lysis was performed by adding 500 µL of lysis buffer per tube, followed by incubation for 10 min at room temperature. Samples were centrifuged at 476 × g for 5 min at 4 °C, washed with cold PBS, and residual supernatant was removed by rapid flicking.

For immunostaining, antibody mixes were prepared and added at appropriate volumes, followed by incubation for 30 min at 4 °C in the dark. Unstained and fluorescence minus one (FMO) controls were included to define instrument settings and establish gating strategies. The following antibodies were used at a 1:200 dilution: CD45-VioGreen (Cat# 130-110-803), CD11b-FITC (Cat# 130-110-803), Ly6G-VioBlue (Cat# 130-119-986), Ly6C-APC-Vio770 (Cat# 130-121-439), F4/80-PE-Vio770 (Cat# 130-118-320), and MHC-II-APC (Cat# 130-102-139) (Miltenyi Biotec, Bologna, Italy), as well as CD206-PE (Cat# 141706; BioLegend, San Diego, CA, USA).

Data acquisition was performed on a BD FACSVerse flow cytometer, collecting 500,000 $CD45^+$ events per sample. Acquisition and analysis were carried out using BD FACSSuite software. For analysis, cells were initially gated based on forward and side scatter parameters to exclude debris. Venus expression was measured as an internal control for tumor cell content and Venus-positive cells represented on average approximately 50% of the tumor bulk. Dead cells were excluded using 7-AAD staining (Miltenyi Biotec; Cat# 170-081-088) and $CD45^+$ leukocytes were subsequently selected. Immune cell subsets were defined as follows: $CD11b^+Ly6G^+$ polymorphonuclear myeloid-derived suppressor cells (PMN-MDSCs), $CD11b^+Ly6C^+$ monocytic MDSCs (M-MDSCs), $CD11b^+F4/80^+MHC\text{-}II^+$ M1 macrophages, $CD11b^+F4/80^+CD206^+$ M2 macrophages and $CD11b^+F4/80^+MHC\text{-}II^-CD206^-$ M0 macrophages. Data are presented as percentage of CD45 + cells. Five tumors per group were analyzed, and statistical significance was assessed using the Mann-Whitney test. This analysis was exploratory and was performed only in the independent replicate cohort.

Monocyte isolation from human PBMCs

Human monocytes were isolated from peripheral blood mononuclear cells (PBMC) obtained from commercially available human buffy coats from healthy donors. To minimize donor-dependent variability, buffy coats from three female donors were pooled before processing. PBMCs were isolated using a no-touch procedure to avoid unintended cell activation or phenotypic alteration [62]. Briefly, blood components were separated by density-gradient centrifugation using Ficoll-Paque Plus (Sigma) for 30 min at 900 x g. The PBMC ring was harvested, and residual erythrocytes were removed using ACK Lysing Buffer (Thermo Fisher Scientific). Monocytes were subsequently plated at a density of 6 × 10^6 cells/cm^2 in serum-free medium to remove lymphocyte and dendritic cell contamination by exploiting the intrinsic adhesive properties of monocytes/macrophages [62]. After 15 min of incubation at 37 °C in a humidified atmosphere and 5% CO2, the non-adherent cells were removed by medium replacement, and the monocytes were cultured in complete RPMI 1640 medium supplemented with 10% heat-inactivated Fetal Bovine Serum, GlutaMAX™ (Thermo Fisher Scientific), and 1% Penicillin-Streptomycin (10,000 U/mL) (Thermo Fisher Scientific).

Macrophage differentiation and polarization

Primary human monocytes were differentiated into unpolarized macrophages (M0) macrophage by culture in the presence of human macrophage colony-stimulating factor (M-CSF; 20 ng/ml; AF-300-25, PeproTech). Cells were cultured for a total of 7 days, with medium renewal on days 3 and 5. To induce polarization, at the final medium change, the M-CSF-containing medium was supplemented with tumor necrosis factor-α (TNF-α; 100ng/ml; 210-TA, Bio-Techne) and interferon-γ (IFN-γ; 20ng/ml; 285-IF, Bio-Techne) to generate M1-like pro-inflammatory macrophages, or with interleukin-4 (IL-4; 40ng/ml; 204-IL, Bio-Techne) and interleukin-13 (IL-13; 20ng/ml; 213-ILB, Bio-Techne) to generate M2-like anti-inflammatory macrophages [63, 84, 85].

Macrophage phenotypic and morphological characterization

Flow cytometric analysis of macrophage phenotype

Macrophages immunophenotype was assessed by flow cytometry analysis of established surface markers. Classically activated M1-like macrophages were identified by the expression of CD80 and HLA-DR, whereas alternatively activated M2-like macrophages were identified by the expression of CD163 and CD206 [86].

Macrophages were detached using StemPro Accutase Cell Dissociation Reagent (Thermo Fisher Scientific) and collected by centrifugation at 300 x g for 10 min. Cell pellets were resuspended in FACS buffer consisting of phosphate-buffered saline supplemented with 0,5% Bovine Serum Albumin (BSA; A7906, Sigma Aldrich) and 2mM EDTA (Thermo Fisher Scientific), and incubated with human FcR Blocking Reagent (Miltenyi Biotec) to minimize nonspecific antibody binding. Dead cells were excluded using LIVE/DEAD Fixable Aqua Dead Cell Stain Kit (1:100 dilution; Thermo Fisher Scientific). After washing, cells were incubated for 30 min on ice, protected from light, with saturating concentration of the following fluorochrome-conjugated antibodies: PE/Cyanine7 anti-human CD80 (clone 2D10, 1:160, Bio Legend), PerCP/Cyanine5.5 anti-human HLA-DR (lone LN3, 1:160, Bio Legend), Alexa Fluor 647 anti-human CD163 (clone GHI/61, 1:300, BD Bioscience), and PE anti-human CD206/MMR (clone 15−2, 1:300, Bio Legend). Doublets were excluded from the analysis to minimize false positive events and Fluorescence minus one (FMO) control was used as negative staining control. Data were acquired on a FACSCanto Flow Cytometer (BD Biosciences) with 10,000 events collected per condition and analyzed using FlowJo software (BD Biosciences).

Confocal imaging of macrophage morphology

Macrophage morphology was assessed by confocal fluorescence microscopy. Cells were seeded on glass coverslips, fixed with 4% paraformaldehyde (043368.9 M, Thermo Fisher Scientific) and stained with Phalloidin Alexa Fluor 488 (A12379, Thermo Fisher Scientific) to visualize the actin cytoskeleton and Hoechst 33,342 (H1399, Thermo Fisher Scientific) to label nuclei. Coverslips were mounted in ProLong™ Diamond Antifade Mountant (P36961, Thermo Fisher Scientific) and imaged using Olympus Fluoview FV3000 confocal laser-scanning microscope under identical acquisition settings for all conditions.

Transmission electron microscopy of macrophage ultrastructure

Samples were fixed using a solution containing 2.5% glutaraldehyde in 0.1 M cacodylate buffer at pH 7.3 for 1 h. After fixation, the samples underwent a series of washing steps and were post-fixed with 1% buffered osmium tetroxide for 1 h at 4 °C. Subsequently, the samples were stained overnight at 4 °C with 0.5% Millipore-filtered uranyl acetate. Dehydration was performed using increasing concentrations of ethanol, followed by infiltration and embedding in Epon. Polymerization was carried out at 60 °C for 48 h. Ultrathin sections were obtained using a Leica EM FC7 ultramicrotome. After staining with uranyl acetate and lead citrate, the sections were analyzed using a TALOS L120C Transmission Electron Microscope (Thermo Fisher Scientific), and images were acquired with a CETA 4 × 4k CMOS camera (Thermo Fisher Scientific).

Cytokine profiling

Macrophage-conditioned media were analyzed using Proteome Profiler Human XL Cytokine Array Kit (ARY022B, Bio-Techne), according to manufacturer's instructions to profile cytokine abundance. Briefly, cytokine array membranes were blocked, incubated overnight at 4 °C with conditioned media, and subsequently probed with the manufacturer-provided detection antibody cocktail and streptavidin-HRP according to manufacturer's instructions. Chemiluminescent signals were developed using ECL detection kit (Amersham Biosciences)

with a BioRad ChemiDoc MP Imaging System (Bio-Rad). For display purposes, image exposure was uniformly adjusted to −0.5; quantification was performed on unadjusted raw images.

CXCL10 neutralization in conditioned media

To assess the contribution of the macrophage-derived cytokines, macrophage M1-like conditioned medium was incubated with neutralizing monoclonal antibody against human CXCL10/IP-10 (MAB266, Bio-Techne) for 1 h at room temperature prior to administration to target cells. Antibody treated conditioned medium, and relative controls, were then applied to MDA-MB-231 cells under the indicated experimental conditions.

RNA interference

CXCR3 knockdown was achieved by two sequential rounds of reverse transfection performed 48 h apart using Silencer Pre-Designed siRNA against CXCR3 (AM16704, Thermo Fisher Scientific) or Stealth RNAi siRNA Negative Control Low GC (1293200, Thermo Fisher Scientific). For each 100 mm dish, Lipofectamine RNAiMAX (13778075, Thermo Fisher Scientific) and siRNA were diluted separately in Opti-MEM (11058021, Thermo Fisher Scientific), combined at a 3:1 ratio according to manufacturer's instruction, and incubated for 20 min at room temperature before addition to cells. Culture medium was replaced the day after, and silencing efficiency was evaluated 96 h after the first transfection.

Flow cytometric analysis of cell cycle distribution

MDA-MB-231 cells were seeded in a 60 mm dish and treated with the different macrophage-conditioned media for 48 h. Following treatment, cells were harvested, centrifuged, and fixed in 70% ethanol for 1 h in ice. Fixed cells were then pelleted and resuspended in staining solution containing propidium iodide (50 µg/ml; P4170, Merck), RNAse A (0,1 mg/ml; EN0531, Thermo Fisher Scientific) and 0,05% Triton X-100 for 40 min at 37 °C. After staining, cells were resuspended in FACS buffer prior to acquisition.

Samples were acquired on a BD FACSCanto flow cytometer (BD Biosciences), and DNA content was analyzed by measuring linear PE fluorescence intensity versus cell count. Cell cycle distribution was quantified using the univariate Cell Cycle modeling tool in FlowJo software (BD Biosciences).

Flow cytometric analysis of apoptosis

MDA-MB-231 cells were seeded in 60 mm dishes and treated with the different macrophage-conditioned media for 48 h. After treatment, both suspended and adherent cells were harvested and processed for apoptotic cell detection using CellEvent Caspase-3/7 Green Flow Cytometry Assay Kit (C10427, Thermo Fisher Scientific), according to manufacturer's instructions. Briefly, cell pellets were resuspended in staining solution containing a 1:1000 dilution of the CellEvent Caspase-3/7 Green Detection Reagent and incubated for 30 min at 37 °C. After staining, cells were washed and resuspended in FACS buffer prior to flow cytometry acquisition.

Samples were acquired on a BD FACSCanto flow cytometer (BD Biosciences), and the percentage of caspase-3/7-positive cells was determined. Data were analyzed using FlowJo software (BD Biosciences).

Western blotting

Following the indicated treatments, cells were washed with ice-cold PBS and lysed in RIPA buffer (25 mM Tris-HCl pH 7.6, 150 mM NaCl, 1% Sodium deoxycholate, 1% Triton X-100, 1% IGEPAL CA630, 0,1% SDS, 2 mM EDTA dihydrate) supplemented with protease and phosphatase inhibitor (78444, Thermo Fisher Scientific). Samples were incubated on a rotating wheel for 30 min at 4 °C and clarified by centrifugation at 12,000 x g for

15 min at 4 °C. Protein concentration was determined using the BCA Protein Assay Kit (23225, Thermo Fisher Scientific).

Equal amounts of proteins were separated by SDS-PAGE at 10% and transferred to nitrocellulose membranes (GE10600003, Amersham). Membranes were blocked in 5% bovine serum albumin (A7906, Thermo Fisher Scientific) in PBS containing 0.1% Tween-20 and incubated overnight at 4 °C with the following primary antibodies: ATF4 (1:800, 97038, Cell Signaling); p-eIF2α (Ser51; 1:800, 3398, Cell Signaling); eIF2α (1:1000; E0157, Sigma Aldrich); CXCR3 (1:1000; MAB160, Bio-Techne); b-actin (1:10000; A5441-.2ML, Sigma Aldrich); GAPDH (1:10000; MA5-15738-HRP, Thermo Fisher Scientific). After washing, membranes were incubated for 45 min at RT with HRP-conjugated secondary antibodies (anti-mouse IgG, 7076, Cell Signaling or anti-rabbit IgG, 7074 Cell Signaling). Membranes were then developed using ECL detection kit (1705061, Bio-Rad) and images were acquired via ChemiDoc MP imaging system (Bio-Rad). Band intensity was quantified via ImageLab software. For display purposes, image exposure was uniformly adjusted to −0.5; quantification was performed on unadjusted raw images. All the uncropped Western Blot belonging to Amin Figures and Supplementary Figures are collected in the file Supplementary 2_Uncropped Western Blots.

RNA extraction and RT-qPCR

Total RNA was extracted from cells using the RNeasy Mini Kit (74106, Qiagen). Reverse transcription was performed from 1 µg of total RNA using the QuantiTect Reverse Transcription Kit (205314, Qiagen), according to manufacturer's instructions. RT-qPCR was carried out using SYBR Green PCR Master Mix (4334973, Thermo Fisher Scientific) on a ViiA 7 Real-Time PCR System (Thermo Fisher Scientific). Gene-specific primers were designed using NCBI Primer-BLAST. Melting curve analysis was performed to confirm amplification specificity, Relative mRNA expression was calculated using the 2^-ΔΔCt method and normalized to GAPDH expression.

MMP9: Forward primer (5'→3'): ATT TCT GCC AGG ACC GCT TCT ACT, Reverse primer (5'→3'): CAG TTT GTA TCC GGC AAA CTG GCT. GAPDH: Forward primer (5'→3'): GGT CTC CTC TGA CTT CAA CA, Reverse primer (5'→3'): AGC CAA ATT CGT TGT CAT AC.

Immunofluorescence microscopy and image analysis

Cells were seeded on 13 mm glass coverslips and, following the indicated experimental procedures, fixed in 4% paraformaldehyde (043368.9 M, Thermo Fisher Scientific) for 15 min at room temperature. Cells were then permeabilized with 0.1% Triton X-100 for 10 min and blocked with 5% bovine serum albumin (BSA; A7906, Thermo Fisher Scientific) for 1 h at room temperature. Samples were incubated overnight at 4 °C with anti-ATF4 primary antibody (1:100, 97038, Cell Signaling). After washing in PBS, samples were incubated for 1 h at room temperature with a goat anti-mouse Alexa Fluor Plus 647 secondary antibody (1:3000; A32728, Thermo Fisher Scientific) and Hoechst 33,342 (1:10000; H3570, Thermo Fisher Scientific).

Images were acquired using an Olympus FluoView FV3000RS confocal microscope and processed with Fiji software for morphological analyses and fluorescence quantification. ATF4 signal was quantified at the single cell level from confocal images. Nuclear masks were generated using Cellpose [87] with a diameter parameter of 30. Raw images and the corresponding nuclear masks were imported into MATLAB for quantification with custom written routines. Mean nuclear ATF4 fluorescence intensity was measured for each cell, excluding nuclei detected at the image borders and nuclei with an area smaller than 5 μm^2. Data from individual fields were then grouped by treatment.

EdU incorporation assay

MDA-MB-231 cells were seeded on coverslips and exposed to the indicated macrophage-conditioned media for 48 h. During the final 3 h of treatment, cells were pulsed with 20 µM EdU and subsequently processed with

EdU Proliferation Kit (iFluor 488; ab219801, Abcam) according to the manufacturer's instructions. Nuclei were counterstained with Hoechst 33,342 (1:10000; H3570, Thermo Fisher Scientific). Representative images were acquired using an Olympus FluoView FV3000RS confocal microscope. Images used for quantification were acquired using a Crest X-Light V3 Deep SIM spinning disk confocal microscope (CrestOptics) and processed in Fiji. EdU fluorescence was quantified at single-cell level. Nuclear masks were generated using Cellpose [87] with a diameter parameter of 30. Raw images and the corresponding nuclear masks were imported into MATLAB for quantification with custom-written routines. Mean nuclear EdU fluorescence intensity was measured for each cell, excluding nuclei detected at image borders and nuclei with an area smaller than 5 μm^2. Data from individual fields were then grouped by treatment. A fluorescence threshold of 500 a.u. was applied to distinguish EdU-positive from EdU-negative nuclei. EdU-positive cells were plotted as a percentage of the total Hoechst-positive nuclei.

Nanolive label-free live-cell imaging

Viable and apoptotic cells were monitored using a CX96 holotomographic microscope (Nanolive). Cells were seeded in the LIVE96 Imaging Lid and, after exposure to the indicated macrophage-conditioned media, subjected to the marker-free LIVE Cytotoxicity Assay for 72 h. Images were acquired hourly and viable and apoptotic cells were analyzed using the LIVE Cytotoxicity Assay module in EVE software (Nanolive). Parameters were exported as hourly group means and SD from six experimental replicates per condition. Data were processed in R (v4.5.0), and SD values were converted to SE as SD/√6. Temporal profiles were displayed using the Savitzky–Golay-smoothed values exported by the Nanolive software. At the final time point, each treatment was compared with the untreated control using two-sided Welch's t-tests reconstructed from the exported means, SD values, and sample sizes. *P* values were adjusted within each parameter using the Benjamini–Hochberg procedure.

3D invasion assay in a microfluidic chip

MDA-MB-231 cell invasion was assessed using the idenTX 3 microfluidic device (Aim Biotech), according to manufacturer's instructions. The central gel channel was filled with Collagen I (3 mg/ml; 354249, SIAL) and allowed to polymerize for 30 min at 37 °C. MDA-MB-231 cells (50000 cells/device) were seeded in one lateral channel, whereas the opposite channel was filled with complete culture medium supplemented with additional 10% FBS as chemoattractant. After 8 h to allow cell adhesion, cells were treated in the seeding channel with conditioned media and/or drugs as indicated. Fixation in 4% paraformaldehyde was performed 48 h after treatment, and nuclei were stained with propidium iodide (0,3 µg/ml; P4170, Merck), to avoid interference from device autofluorescence in the 405 nm channel, and with Phalloidin Alexa Fluor 488 (A12379, Thermo Fisher Scientific) to visualize the actin cytoskeleton. Following immunofluorescence staining, z-stack images were acquired using an Olympus FluoView FV3000RS confocal microscope with a 10x objective and a 4 µm z-step. For each device, three independent fields spanning the cell and gel channels were imaged.

Images were analyzed using a custom Fiji macro. Briefly, nuclei z-stacks were projected into a single plane using the Z projection command and adjusted for brightness and contrast. Before image binarization, a Gaussian blur filter was applied to define cell outlines, and the watershed function was used to separate closely apposed nuclei. Three regions of interest (ROI) per image were defined on the brightfield channel, extending from the base of the triangular post to the maximum distance reached by invading cells within the collagen channel. These ROIs were then transferred to the nuclei channel, and invading cells were quantified using the Analyze Particles function. Invasion was expressed as both the number of invaded cells and the distance traveled from the edge of the gel channel.

Bulk RNA sequencing

Transcriptomic profiling under chemical stress conditions was performed in biological triplicate using MDA-MB-231 cells treated with Sephin1 (10 µM) for 48 h and using vehicle-treated cells as controls.

Total RNA was extracted using the RNeasy Mini Kit (74106, Qiagen) and RNA concentration was quantified by Qubit fluorometric assay. RNA purity was assessed spectrophotometrically with an Epoch microplate reader, while integrity was evaluated using a Fragment Analyzer prior to library preparation. Poly(A)-selected mRNA libraries were generated using the Standard Input mRNA NovaSeq6000Gb library protocol, targeting 2 × 150 bp reads, and sequenced on the Illumina NovaSeq 6000 platform (Illumina, San Diego, CA, USA). Raw read quality was assessed using FastQC (v0.12.1; https://www.bioinformatics.babraham.ac.uk/projects/fastqc) and reports were aggregated with MultiQC (v1.28) [88]. Reads were aligned to the human reference genome (GRCh38) using STAR (v2.7.10b) [89], and gene-level counts were generated with FeatureCounts (v2.0.8) [90].

into R (v4.3.2) and processed with the DESeq2 workflow (v1.42.1) [91]. Sample distribution and clustering were initially evaluated by principal component analysis (PCA) to check samples clustering according to their phenotype. Genes were considered differentially expressed when the adjusted P value was < 0.05 and the absolute log2FoldChange was ≥ 0.58, corresponding to a fold change of at least 1.5 in either direction.

TCGA-BRCA, METABRIC and stress signatures analysis

TCGA-BRCA bulk tumor RNA-sequencing data were obtained from the Genomic Data Commons using TCGAbiolinks. Harmonized STAR-Counts files were processed from the unstranded assay, normalized by the trimmed mean of M values in edgeR, and converted to log2 CPM values. Clinical annotations were retrieved from matched TCGA metadata, and overall survival was defined from days_to_death or days_to_last_follow_up, as appropriate. Molecular subtypes were derived from PAM50 annotations and collapsed into a 3-class framework comprising ER/PR+ (Luminal A, Luminal B, and Normal-like), HER2+ (HER2-enriched), and TNBC (Basal-like) tumors. METABRIC expression and clinical annotations were obtained from the published cohort [33]. Overall survival, relapse-free survival, and disease-specific survival were evaluated with high- and low-score groups defined using maximally selected rank statistics, and survival differences were assessed by two-sided log-rank tests.

The curated Metabolic Stress [9] and Chemical Stress signatures, together with the Bindea immune signatures and the identifiers and source publications for the additional microenvironmental stress signatures, are provided in Supplementary Table 1, together with the additional signatures representing ISR activation. Sample-level activity was quantified by ssGSEA on log2 counts-per-million expression values. Associations among signatures were assessed by Spearman correlation, and TNBC scores were compared with the other molecular subtypes. For Hallmark pathway analysis, genes were ranked by Pearson correlation with the indicated ISR signature and subjected to pre-ranked GSEA against MSigDB Hallmark gene sets.

Immune-cell transcriptional programs were quantified by ssGSEA using GSVA and the published Bindea signatures [33]. Relative immune-cell fractions were independently inferred using CIBERSORTx with the LM22 reference matrix [34]. Associations among stress scores, immune programs, and inferred cell fractions were assessed by Spearman correlation, with Benjamini-Hochberg correction where indicated. Ranked moving-average plots used a 10-sample sliding window.

All analyses were performed in R (version 4.5.0) using RStudio (version 2024.12.1+563; Posit Software, PBC). Key packages included TCGAbiolinks, edgeR, GSVA, clusterProfiler, msigdbr, survminer, ComplexHeatmap, ppcor, and tidyverse; complete session information is available upon request.

Public metastatic transcriptomic dataset analyses

Processed GSE121945 expression data comprised three biological replicates each of FACS-isolated CXCR3-negative and CXCR3-positive SUM-LM1 cells. Expression values and the Chemical Stress score were compared

by two-sided unpaired t tests. Competitive enrichment of independent ISR- and ATF4-related gene sets was evaluated with Correlation Adjusted MEan Rank (CAMERA); bar direction indicates enrichment in CXCR3-positive cells.

For GSE241165, processed single-cell counts from 4T1 cells collected in vitro, from mammary fat-pad tumors, and from bone at days 4, 10, and 16 after intracardiac injection were analyzed. Cells were classified as CXCR3-positive when Cxcr3 expression was detected and otherwise as CXCR3-negative. ISR Core 19 and Metabolic Stress activities were calculated per cell with UCell, and CXCR3 groups were compared within each stage by two-sided Wilcoxon rank-sum tests.

Statistical analyses

Unless otherwise specified, experiments included at least three independent biological replicates. For all experiments, two-group comparisons used two-sided Mann-Whitney tests, and comparisons involving more than two groups used Kruskal-Wallis tests. For GSE121945, expression and signature scores were compared using two-sided unpaired t tests and competitive gene-set testing was performed with CAMERA. Single-cell comparisons in GSE241165 used two-sided Wilcoxon rank-sum tests. Outliers were identified using the ROUT method and excluded.

Differences were considered statistically significant at $p<0.05$ (*), $p<0.01$ (**), $p<0.001$ (***) and $p<0.0001$ (****). Data are presented as mean ± SD unless otherwise indicated.

Supplementary Information The online version contains supplementary material available at https://doi.org/10.1186/s13046-026-03821-4.

Acknowledgements We thank Prof Giampaolo Bianchini (Vita-Salute San Raffaele University, Milan) and Dr Silvia Lopa (Cell and Tissue Engineering Laboratory, IRCCS Ospedale Galeazzi-Sant'Ambrogio, Milan) for helpful discussions and critical reading of the manuscript. We are grateful to ALEMBIC (Advanced Light and Electron Microscopy BioImaging Center, IRCCS San Raffaele Scientific Institute) for imaging support, FRACTAL (Flow cytometry Resource, Advanced Cytometry Technical Applications Laboratory core facility, IRCCS Ospedale San Raffaele) for flow cytometry support and COSR (Center for Omics Sciences, IRCCS Ospedale San Raffaele) for bioinformatic support.

Authors' contributions MC conceived the study together with CT and PF, participated in the study design, carried out cell culture experiments, macrophage-conditioned medium experiments, invasion assays, western blotting and immunofluorescence analyses, performed part of the data analysis, prepared figures and drafted the manuscript. VS carried out in vivo experiments, including the orthotopic mouse model, tumour growth monitoring and immune infiltration analyses, and contributed to methodology and data visualization. JC carried out bioinformatic analyses, including TCGA-BRCA analyses, ISR signature scoring and survival analyses, performed formal analyses and contributed to figure preparation. EC contributed to imaging analysis methodology, performed formal analyses and contributed to figure preparation. ALo performed imaging and electron microscopy acquisition and analyses and contributed to data visualization. ALa carried out histology-based metastatic burden analyses, including lung metastasis quantification, and contributed to data visualization. CC contributed to biochemical and imaging analyses and to data visualization. ML contributed to biochemical and imaging analyses and to data visualization. EL contributed to the development of the engineered cell lines and to methodology. MG contributed to the development of the engineered cell lines, biochemical analyses and methodology. FG carried out computational analyses, performed formal analyses and contributed to methodology. AA contributed to flow cytometry-based macrophage characterization and immune profiling, and contributed to methodology and data visualization. DM supervised imaging analyses and contributed to data interpretation. MI supervised metastatic burden analyses and contributed to data interpretation. CG supervised experimental and bioinformatic analyses and contributed to data interpretation. PD supervised the in vivo analyses, contributed to methodology development and data interpretation. CT conceived the study together with MC and PF, participated in study design and coordination, supervised the imaging and methodological aspects of the study, acquired funding and contributed to manuscript revision. PF conceived the study together with MC and CT, participated in study design and coordination, supervised the experimental and analytical work, performed part of the formal analyses, prepared figures and drafted the manuscript. All authors contributed to manuscript revision, read and approved the final manuscript.

Funding This work was supported by PRIN 2020 (2020RRJP5L_005) to CT. PF was supported by Fondazione Veronesi postdoctoral fellowships (3311 and 4179) and MC was supported by Fondazione Umberto Veronesi postdoctoral fellowships

(5094, 5317 and 54542).

Data availability The RNA-sequencing data generated in this study for chemical stress conditions in TNBC cells have been deposited in the Gene Expression Omnibus (GEO) under accession number GSE327254. Public datasets reanalyzed in this study are available under GSE121945 (within GSE121947) and GSE241165. All other data supporting the findings of this study are available within the paper and its Supplementary Information or available from the author upon reasonable request.

Declarations

Ethics approval and consent to participate Mice were bred and maintained under saprophytic and pathogen-free conditions at the animal facilities of the Molecular Biotechnology Center (University of Torino) and treated in accordance with EU and institutional guidelines. This study fully complied with the ethical principles of the Three Rs (3Rs) to Replace, Reduce and Refine the use of animals in research, as required by national and international rules and is provided by Italian Ministry of Health authorization number CC652.72.

Consent for publication Not applicable.

Competing interests The authors declare no competing interests.

References

1. Gerstberger S, Jiang Q, Ganesh K. Metastasis Cell. 2023;186:1564–79.
2. Swanton C, Bernard E, Abbosh C, André F, Auwerx J, Balmain A, et al. Embracing cancer complexity: Hallmarks of systemic disease. Cell. 2024;187:1589–616.
3. Massagué J, Obenauf AC. Metastatic colonization by circulating tumour cells. Nature. 2016;529:298–306.
4. Hagan CE, Sheehan VM, Rezanka CM, Li MA, Martínez-Escardó L, Campbell KJ, et al. Apoptotic cells promote circulating tumor cell survival and metastasis. Commun Biol. 2025;8:1121.
5. Basnet H, Tian L, Ganesh K, Huang Y-H, Macalinao DG, Brogi E, et al. Flura-seq identifies organ-specific metabolic adaptations during early metastatic colonization. eLife. 2019;8:e43627.
6. Mavuluri J, Dhungana Y, Jones LL, Bhatara S, Shi H, Yang X, et al. GPR65 Inactivation in Tumor Cells Drives Antigen-Independent CAR T-cell Resistance via Macrophage Remodeling. Cancer Discov. 2025;15:1018–36.
7. Wang W, Taufalele PV, Millet M, Homsy K, Smart K, Berestesky ED, et al. Matrix stiffness regulates tumor cell intravasation through expression and ESRP1-mediated alternative splicing of MENA. Cell Rep. 2023;42:112338.
8. García-Jiménez C, Goding CR. Starvation and Pseudo-Starvation as Drivers of Cancer Metastasis through Translation Reprogramming. Cell Metab. 2019;29:254–67.
9. Falletta P, Sanchez-Del-Campo L, Chauhan J, Effern M, Kenyon A, Kershaw CJ, et al. Translation reprogramming is an evolutionarily conserved driver of phenotypic plasticity and therapeutic resistance in melanoma. Genes Dev. 2017;31:18–33.
10. Licari E, Sánchez-del-Campo L, Falletta P. The two faces of the Integrated Stress Response in cancer progression and therapeutic strategies. Int J Biochem Cell Biol. 2021;139:106059.
11. Yeh H, DelGaudio NL, Uygur B, Millet A, Khan A, Unlu G, et al. Mitochondrial Glutathione Import Enables Breast Cancer Metastasis via Integrated Stress Response Signaling. Cancer Discov. 2025;15:2437–49.
12. Pakos-Zebrucka K, Koryga I, Mnich K, Ljujic M, Samali A, Gorman AM. The integrated stress response. EMBO Rep. 2016;17:1374–95.
13. Tang H, Kang R, Liu J, Tang D. ATF4 in cellular stress, ferroptosis, and cancer. Arch Toxicol. 2024;98:1025–41.

14. Wu D, Liang J. Activating transcription factor 4: a regulator of stress response in human cancers. Front Cell Dev Biol. 2024;12:1370012.
15. Zinszner H, Kuroda M, Wang X, Batchvarova N, Lightfoot RT, Remotti H, et al. CHOP is implicated in programmed cell death in response to impaired function of the endoplasmic reticulum. Genes Dev. 1998;12:982–95.
16. Fawcett TW, Martindale JL, Guyton KZ, Hai T, Holbrook NJ. Complexes containing activating transcription factor (ATF)/cAMP-responsive-element-binding protein (CREB) interact with the CCAAT/enhancer-binding protein (C/EBP)-ATF composite site to regulate Gadd153 expression during the stress response. Biochem J. 1999;339(Pt 1):135–41.
17. Patel AAH, Dzanan JJ, Ali KX, Eklund EA, Alvarez SW, Raj D et al. Ageing promotes metastasis via activation of the integrated stress response. Nature. 2026 ; Available from: https://www.nature.com/articles/s41586-026-10216-0. [Cited 20 Mar 2026].
18. Vivas-García Y, Falletta P, Liebing J, Louphrasitthiphol P, Feng Y, Chauhan J, et al. Lineage-Restricted Regulation of SCD and Fatty Acid Saturation by MITF Controls Melanoma Phenotypic Plasticity. Mol Cell. 2020;77:120–e1379.
19. Lu S, Yang L-X, Cao Z-J, Zhao J-S, You J, Feng Y-X. Transcriptional Control of Metastasis by Integrated Stress Response Signaling. Front Oncol. 2021;11:770843.
20. Bianchini G, Balko JM, Mayer IA, Sanders ME, Gianni L. Triple-negative breast cancer: challenges and opportunities of a heterogeneous disease. Nat Rev Clin Oncol. 2016;13:674–90.
21. Furukawa N, Stearns V, Santa-Maria CA, Popel AS. The tumor microenvironment and triple-negative breast cancer aggressiveness: shedding light on mechanisms and targeting. Expert Opin Ther Targets. 2022;26:1041–56.
22. Medrek C, Pontén F, Jirström K, Leandersson K. The presence of tumor associated macrophages in tumor stroma as a prognostic marker for breast cancer patients. BMC Cancer. 2012;12:306.
23. Yuan Z-Y, Luo R-Z, Peng R-J, Wang S-S, Xue C. High infiltration of tumor-associated macrophages in triple-negative breast cancer is associated with a higher risk of distant metastasis. OncoTargets Ther. 2014;7:1475–80.
24. Ye J, Wang X, Shi J, Yin X, Chen C, Chen Y, et al. Tumor-associated macrophages are associated with response to neoadjuvant chemotherapy and poor outcomes in patients with triple-negative breast cancer. J Cancer. 2021;12:2886–92.
25. Borriello L, Coste A, Traub B, Sharma VP, Karagiannis GS, Lin Y, et al. Primary tumor associated macrophages activate programs of invasion and dormancy in disseminating tumor cells. Nat Commun. 2022;13:626.
26. Hirano R, Okamoto K, Shinke M, Sato M, Watanabe S, Watanabe H, et al. Tissue-resident macrophages are major tumor-associated macrophage resources, contributing to early TNBC development, recurrence, and metastases. Commun Biol. 2023;6:144.
27. Sica A, Mantovani A. Macrophage plasticity and polarization: in vivo veritas. J Clin Invest. 2012;122:787–95.
28. Coulton A, Murai J, Qian D, Thakkar K, Lewis CE, Litchfield K. Using a pan-cancer atlas to investigate tumour associated macrophages as regulators of immunotherapy response. Nat Commun. 2024;15:5665.
29. Murray PJ, Allen JE, Biswas SK, Fisher EA, Gilroy DW, Goerdt S, et al. Macrophage Activation and Polarization: Nomenclature and Experimental Guidelines. Immunity. 2014;41:14–20.
30. Gordon S, Martinez FO. Alternative Activation of Macrophages: Mechanism and Functions. Immunity. 2010;32:593–604.
31. Vitale I, Manic G, Coussens LM, Kroemer G, Galluzzi L. Macrophages and Metabolism in the Tumor Microenvironment. Cell Metab. 2019;30:36–50.
32. Das I, Krzyzosiak A, Schneider K, Wrabetz L, D'Antonio M, Barry N, et al. Preventing proteostasis diseases by selective inhibition of a phosphatase regulatory subunit. Science. 2015;348:239–42.
33. Group METABRIC, Curtis C, Shah SP, Chin S-F, Turashvili G, Rueda OM, et al. The genomic and transcriptomic architecture of 2,000 breast tumours reveals novel subgroups. Nature. 2012;486:346–52.
34. Chen H, Pan Y-X, Dudenhausen EE, Kilberg MS. Amino Acid Deprivation Induces the Transcription Rate of the Human Asparagine Synthetase Gene through a Timed Program of Expression and Promoter Binding of Nutrient-responsive Basic Region/Leucine Zipper Transcription Factors as Well as Localized Histone Acetylation. J Biol Chem. 2004;279:50829–39.
35. Corbet C, Pinto A, Martherus R, Santiago de Jesus JP, Polet F, Feron O. Acidosis Drives the Reprogramming of Fatty Acid Metabolism in Cancer Cells through Changes in Mitochondrial and Histone Acetylation. Cell Metab. 2016;24:311–23.
36. Bindea G, Mlecnik B, Tosolini M, Kirilovsky A, Waldner M, Obenauf AC, et al. Spatiotemporal Dynamics of Intratumoral Immune Cells Reveal the Immune Landscape in Human Cancer. Immunity. 2013;39:782–95.
37. Steen CB, Liu CL, Alizadeh AA, Newman AM. Profiling Cell Type Abundance and Expression in Bulk Tissues with CIBERSORTx. In: Kidder BL, editor. Stem Cell Transcr Netw. New York, NY: Springer US; 2020. page 135–57. Available from: http://link.springer.com/ https://doi.org/10.1007/978-1-0716-0301-7_7. [Cited 20 Mar 2026].
38. Koncz G, Jenei V, Tóth M, Váradi E, Kardos B, Bácsi A, et al. Damage-mediated macrophage polarization in sterile inflammation. Front Immunol. 2023;14:1169560.
39. Lehmann BD, Bauer JA, Chen X, Sanders ME, Chakravarthy AB, Shyr Y, et al. Identification of human triple-negative breast cancer subtypes and preclinical models for selection of targeted therapies. J Clin Invest. 2011;121:2750–67.

40. Novoa I, Zeng H, Harding HP, Ron D. Feedback Inhibition of the Unfolded Protein Response by *GADD34* -Mediated Dephosphorylation of eIF2α. J Cell Biol. 2001;153:1011–22.
41. Mehner C, Hockla A, Miller E, Ran S, Radisky DC, Radisky ES. Tumor cell-produced matrix metalloproteinase 9 (MMP-9) drives malignant progression and metastasis of basal-like triple negative breast cancer. Oncotarget. 2014;5:2736–49.
42. Zhu S, Liu H, Sha H, Qi L, Gao D-S, Zhang W. PERK and XBP1 differentially regulate CXCL10 and CCL2 production. Exp Eye Res. 2017;155:1–14.
43. Karin N. CXCR3 Ligands in Cancer and Autoimmunity, Chemoattraction of Effector T Cells, and Beyond. Front Immunol. 2020;11:976.
44. Ranganathan AC, Ojha S, Kourtidis A, Conklin DS, Aguirre-Ghiso JA. Dual function of pancreatic endoplasmic reticulum kinase in tumor cell growth arrest and survival. Cancer Res. 2008;68:3260–8.
45. Park Y, Reyna-Neyra A, Philippe L, Thoreen CC. mTORC1 Balances Cellular Amino Acid Supply with Demand for Protein Synthesis through Post-transcriptional Control of ATF4. Cell Rep. 2017;19:1083–90.
46. Pein M, Insua-Rodríguez J, Hongu T, Riedel A, Meier J, Wiedmann L, et al. Metastasis-initiating cells induce and exploit a fibroblast niche to fuel malignant colonization of the lungs. Nat Commun. 2020;11:1494.
47. Neill G, Masson GR. A stay of execution: ATF4 regulation and potential outcomes for the integrated stress response. Front Mol Neurosci. 2023;16:1112253.
48. Wang X, Zhang T, Zheng B, Lu Y, Liang Y, Xu G et al. Lymphotoxin - β Promotes Bone Colonization and Osteolytic Outgrowth of Indolent Bone Metastatic cells of Breast Cancer. Cell Biology; 2023. Available from: http://biorxiv.org/lookup/doi/https://doi.org/10.1101/2023.08.15.553179. [Cited 7 Aug 2026].
49. Xue J, Schmidt SV, Sander J, Draffehn A, Krebs W, Quester I, et al. Transcriptome-Based Network Analysis Reveals a Spectrum Model of Human Macrophage Activation. Immunity. 2014;40:274–88.
50. Mills CD, Kincaid K, Alt JM, Heilman MJ, Hill AM. M-1/M-2 Macrophages and the Th1/Th2 Paradigm. J Immunol. 2000;164:6166–73.
51. Zhang F, Mears JR, Shakib L, Beynor JI, Shanaj S, Korsunsky I, et al. IFN-γ and TNF-α drive a CXCL10+CCL2+ macrophage phenotype expanded in severe COVID-19 lungs and inflammatory diseases with tissue inflammation. Genome Med. 2021;13:64.
52. Qi X, Kim D, Yoon Y, Jin D, Huang X, Li J, et al. Essential involvement of cross-talk between IFN-γ and TNF-α in CXCL10 production in human THP-1 monocytes. J Cell Physiol. 2009;220:690–7.
53. House IG, Savas P, Lai J, Chen AXY, Oliver AJ, Teo ZL, et al. Macrophage-Derived CXCL9 and CXCL10 Are Required for Antitumor Immune Responses Following Immune Checkpoint Blockade. Clin Cancer Res. 2020;26:487–504.
54. Zhang Y, Zhong F, Liu L. Single-cell transcriptional atlas of tumor-associated macrophages in breast cancer. Breast Cancer Res. 2024;26:129.
55. Tokunaga R, Zhang W, Naseem M, Puccini A, Berger MD, Soni S, et al. CXCL9, CXCL10, CXCL11/CXCR3 axis for immune activation - A target for novel cancer therapy. Cancer Treat Rev. 2018;63:40–7.
56. Zhu G, Yan HH, Pang Y, Jian J, Achyut BR, Liang X, et al. CXCR3 as a molecular target in breast cancer metastasis: inhibition of tumor cell migration and promotion of host anti-tumor immunity. Oncotarget. 2015;6:43408–19.
57. Clark AM, Heusey HL, Griffith LG, Lauffenburger DA, Wells A. IP-10 (CXCL10) Can Trigger Emergence of Dormant Breast Cancer Cells in a Metastatic Liver Microenvironment. Front Oncol. 2021;11:676135.
58. Pe KCS, Saetung R, Yodsurang V, Chaotham C, Suppipat K, Chanvorachote P et al. Triple-negative breast cancer influences a mixed M1/M2 macrophage phenotype associated with tumor aggressiveness. Heymann D, editor. PLOS ONE. 2022;17:e0273044.
59. Benner B, Scarberry L, Suarez-Kelly LP, Duggan MC, Campbell AR, Smith E, et al. Generation of monocyte-derived tumor-associated macrophages using tumor-conditioned media provides a novel method to study tumor-associated macrophages in vitro. J Immunother Cancer. 2019;7:140.
60. Duluc D, Delneste Y, Tan F, Moles M-P, Grimaud L, Lenoir J, et al. Tumor-associated leukemia inhibitory factor and IL-6 skew monocyte differentiation into tumor-associated macrophage-like cells. Blood. 2007;110:4319–30.
61. Lurier EB, Dalton D, Dampier W, Raman P, Nassiri S, Ferraro NM, et al. Transcriptome analysis of IL-10-stimulated (M2c) macrophages by next-generation sequencing. Immunobiology. 2017;222:847–56.
62. Heideveld E, Horcas-Lopez M, Lopez-Yrigoyen M, Forrester LM, Cassetta L, Pollard JW. Methods for macrophage differentiation and in vitro generation of human tumor associated-like macrophages. Methods Enzymol. 2020;632:113–31.
63. Czimmerer Z, Varga T, Poliska S, Nemet I, Szanto A, Nagy L. Identification of novel markers of alternative activation and potential endogenous PPARγ ligand production mechanisms in human IL-4 stimulated differentiating macrophages. Immunobiology. 2012;217:1301–14.
64. Lines CL, McGrath MJ, Dorwart T, Conn CS. The integrated stress response in cancer progression: a force for plasticity and resistance. Front Oncol. 2023;13:1206561.
65. Vendramin R, Katopodi V, Cinque S, Konnova A, Knezevic Z, Adnane S, et al. Activation of the integrated stress response confers vulnerability to mitoribosome-targeting antibiotics in melanoma. J Exp Med. 2021;218:e20210571.

66. Bai X, Ni J, Beretov J, Wasinger VC, Wang S, Zhu Y, et al. Activation of the eIF2α/ATF4 axis drives triple-negative breast cancer radioresistance by promoting glutathione biosynthesis. Redox Biol. 2021;43:101993.
67. Greten FR, Grivennikov SI. Inflammation and Cancer: Triggers, Mechanisms, and Consequences. Immunity. 2019;51:27–41.
68. Jewer M, Lee L, Leibovitch M, Zhang G, Liu J, Findlay SD, et al. Translational control of breast cancer plasticity. Nat Commun. 2020;11:2498.
69. Yang J, Antin P, Berx G, Blanpain C, Brabletz T, Bronner M, et al. Guidelines and definitions for research on epithelial–mesenchymal transition. Nat Rev Mol Cell Biol. 2020;21:341–52.
70. Haerinck J, Goossens S, Berx G. The epithelial–mesenchymal plasticity landscape: principles of design and mechanisms of regulation. Nat Rev Genet. 2023;24:590–609.
71. Yan W, Cao QJ, Arenas RB, Bentley B, Shao R. GATA3 Inhibits Breast Cancer Metastasis through the Reversal of Epithelial-Mesenchymal Transition. J Biol Chem. 2010;285:14042–51.
72. He Q, Jing H, Liaw L, Gower L, Vary C, Hua S, et al. Suppression of Spry1 inhibits triple-negative breast cancer malignancy by decreasing EGF/EGFR mediated mesenchymal phenotype. Sci Rep. 2016;6:23216.
73. Shin SY, Nam J-S, Lim Y, Lee YH. TNFα-exposed Bone Marrow-derived Mesenchymal Stem Cells Promote Locomotion of MDA-MB-231 Breast Cancer Cells through Transcriptional Activation of CXCR3 Ligand Chemokines. J Biol Chem. 2010;285:30731–40.
74. Costa-Mattioli M, Walter P. The integrated stress response: From mechanism to disease. Science. 2020;368:eaat5314.
75. Mukherjee D, Bercz LS, Torok MA, Mace TA. Regulation of cellular immunity by activating transcription factor 4. Immunol Lett. 2020;228:24–34.
76. Iwasaki Y, Suganami T, Hachiya R, Shirakawa I, Kim-Saijo M, Tanaka M, et al. Activating Transcription Factor 4 Links Metabolic Stress to Interleukin-6 Expression in Macrophages. Diabetes. 2014;63:152–61.
77. Yang F, Liu Y, Ren H, Zhou G, Yuan X, Shi X. ER-stress regulates macrophage polarization through pancreatic EIF-2alpha kinase. Cell Immunol. 2019;336:40–7.
78. Yu H, Jiao X, Lv Q, Li L, Du Y, Hu C, et al. ATF4 Contributes to Abdominal Aortic Aneurysm Formation via Modulating M1 Macrophage Polarization and Inflammation. Aging Dis. 2024;16:1691–708.
79. Abdel-Nour M, Carneiro LAM, Downey J, Tsalikis J, Outlioua A, Prescott D, et al. The heme-regulated inhibitor is a cytosolic sensor of protein misfolding that controls innate immune signaling. Volume 365. New York, N.Y.: Science; 2019. p. eaaw4144.
80. Liu M, Guo S, Stiles JK. The emerging role of CXCL10 in cancer (Review). Oncol Lett. 2011;2:583–9.
81. Guo Z, Zhu Z, Lin X, Wang S, Wen Y, Wang L, et al. Tumor microenvironment and immunotherapy for triple-negative breast cancer. Biomark Res. 2024;12:166.
82. Cannon A, Thompson CM, Bhatia R, Kandy RRK, Solheim JC, Batra SK, et al. Contribution of CXCR3-mediated signaling in the metastatic cascade of solid malignancies. Biochim Biophys Acta BBA - Rev Cancer. 2021;1876:188628.
83. Wang X, Zhang Y, Wang S, Ni H, Zhao P, Chen G, et al. The role of CXCR3 and its ligands in cancer. Front Oncol. 2022;12:1022688.
84. Chaintreuil P, Kerreneur E, Bourgoin M, Savy C, Favreau C, Robert G, et al. The generation, activation, and polarization of monocyte-derived macrophages in human malignancies. Front Immunol. 2023;14:1178337.
85. Mondadori C, Chandrakar A, Lopa S, Wieringa P, Talò G, Perego S, et al. Assessing the response of human primary macrophages to defined fibrous architectures fabricated by melt electrowriting. Bioact Mater. 2023;21:209–22.
86. Bernaerts E, Ahmadzadeh K, De Visscher A, Malengier-Devlies B, Häußler D, Mitera T, et al. Human monocyte-derived macrophages shift subcellular metalloprotease activity depending on their activation state. iScience. 2024;27:111171.
87. Stringer C, Wang T, Michaelos M, Pachitariu M. Cellpose: a generalist algorithm for cellular segmentation. Nat Methods. 2021;18:100–6.
88. Ewels P, Magnusson M, Lundin S, Käller M. MultiQC: summarize analysis results for multiple tools and samples in a single report. Bioinformatics. 2016;32:3047–8.
89. Dobin A, Davis CA, Schlesinger F, Drenkow J, Zaleski C, Jha S, et al. STAR: ultrafast universal RNA-seq aligner. Bioinformatics. 2013;29:15–21.
90. Liao Y, Smyth GK, Shi W. featureCounts: an efficient general purpose program for assigning sequence reads to genomic features. Bioinformatics. 2014;30:923–30.
91. Love MI, Huber W, Anders S. Moderated estimation of fold change and dispersion for RNA-seq data with DESeq2. Genome Biol. 2014;15:550.

Authors and Affiliations

Martina Crippa[1,2] · Vincenzo Salemme[3] · Jagat Chauhan[4] · Emanuele Colombo[5] · Alessia Loffreda[2,5] · Alessia Lamolinara[6] · Clara Cardella[1] · Martina Leone[1] · Eugenia Licari[7,8] · Marco Gaviraghi[9] · Francesca Genova[10] · Achille Anselmo[1,11,12] · Davide Mazza[1,2] · Manuela Iezzi[6] · Colin Goding[4] · Paola Defilippi[3] · Carlo Tacchetti[1,2] · Paola Falletta[1,2]

✉ Paola Falletta
falletta.paola@hsr.it

1 Vita-Salute San Raffaele University, Milan, Italy

2 Experimental Imaging Centre, IRCCS Ospedale San Raffaele, Milan, Italy

3 Department of Molecular Biotechnology and Health Science, Università degli Studi di Torino, Torino, Italy

4 Ludwig Cancer Research, University of Oxford, Oxford, UK

5 ALEMBIC, Advanced Light and Electron Microscopy BioImaging Center, Milan, Italy

6 Department of Neurosciences, Imaging and Clinical Sciences, Laboratory of Experimental Pathology and Precision Medicine, Center for Advanced Studies and Technology (CAST), "G. d'Annunzio" University of Chieti-Pescara, Chieti, Italy

7 San Raffaele Telethon Institute for Gene Therapy, IRCCS San Raffaele Scientific Institute, Milan, Italy

8 Division of Genetics and Cell Biology, IRCCS San Raffaele Scientific Institute, Milan, Italy

9 Functional Genomics, Genomics Research Center, Human Technopole, Milan, Italy

10 Center for Omics Sciences, IRCCS San Raffaele Scientific Institute, Milan, Italy

11 FRACTAL - Flow cytometry Resource, Advanced Cytometry Technical Applications Laboratory IRCCS Ospedale San Raffaele, Milan, Italy

12 Spectral Flow Unit; Fondazione Istituto Nazionale di Genetica Molecolare-INGM, Milan, Italy